33

Customized Mass Matrices of 1D Elements

TABLE OF CONTENTS

§33.1. Introduction

Two standard procedures for building finite element mass matrices have been covered in the previous Chapter. Those lead to consistent and diagonally-lumped forms. These models are denoted by $\mathbf{M}_C$ and $\mathbf{M}_L$, respectively, in the sequel. Abbreviations CMM and DLMM, respectively, will be also used. Collectively these take care of many engineering applications in structural dynamics. Occasionally, however, they fall short. The gap can be filled with a more general approach that relies on *templates*. These are algebraic forms that carry free parameters. This approach is covered in this paper using one-dimensional structural elements as expository examples.

The template approach has the virtue of generating a set of mass matrices that satisfy certain *a priori* constraints such as symmetry, nonnegativity, invariance and momentum conservation. In particular, the diagonally-lumped and consistent mass matrices can be obtained as instances. Thus those standard models are not excluded. Availability of free parameters, however, allows the mass matrix to be *customized* to special needs such as high precision in vibration analysis, or minimally dispersive wave propagation. This versatility will be evident from the examples. The set of parameters is called the *template signature*, and uniquely characterizes an element instance.

An attractive feature of templates for FEM programming is that each "custom mass matrix" need not be coded and tested individually. It is sufficient to implement the template as a single element-level module, with free parameters as arguments, and simply adjust the signature to the problem at hand. In particular the same module should be able to produce the conventional DLMM and CMM models, which can provide valuable crosschecks.

§33.2. Customization Scenarios

The ability to customize the mass matrix is not free of cost. The derivation is more complicated, even for 1D elements, than those based on standard procedures. In fact, hand computations rapidly become unfeasible. Help from a computer algebra system (CAS) is needed to complete the task. When is this additional work justified? Two scenarios can be mentioned.

The first is *high fidelity systems*. Dynamic analysis covers a wide range of applications. There is a subclass that calls for a level of simulation precision beyond that customary in engineering analysis. Examples are deployment of precision structures, resonance analysis of machinery or equipment, adaptive active control, ultrasonics imaging, signature detection, radiation loss in layered circuits, and molecular- and crystal-level simulations in micro- and nano-mechanics.

In structural static analysis an error of 20% or 30% in peak stresses is not cause for alarm — such discrepancies are usually covered adequately by safety factors. But a similar error in frequency analysis or impedance response of a high fidelity system may be disastrous. Achieving acceptable precision with a fine mesh, however, can be expensive. Model adaptivity comes to the rescue in statics; but this is less effective in dynamics on account of the time dimension. Customized elements may provide a practical solution: achieving adequate accuracy with a coarse regular mesh.

A second possibility is that the stiffness matrix comes from a method that *avoids displacement shape functions*. For example assumed-stress or assumed strain elements. [Or, it could simply be an array of numbers provided by a black-box program, with no documentation explaining its source.] If this happens the concept of "consistent mass matrix," in which velocity shape functions are taken to coincide with displacement ones, loses its comfortable variational meaning. One way

out is to take the mass of an element with similar geometry and freedom configuration derived with shape functions, and to pair it with the given stiffness. But in certain cases, notably when the FEM model has rotational freedoms, this may not be easy or desirable.

§33.3. Parametrization Techniques

There are several ways to parametrize mass matrices. Three techniques found effective in practice are summarized below. All of them are illustrated in the worked out examples of Sections 4–6.

Matrix-Weighted Parametrization. A matrix-weighted mass template for element e is a linear combination of $(k + 1)$ component mass matrices, $k \geq 1$ of which are weighted by parameters:

$$\mathbf{M}^e \stackrel{\text{def}}{=} \mathbf{M}_0^e + \mu_1 \mathbf{M}_1^e + \ldots \mu_k \mathbf{M}_k^e \tag{33.1}$$

Here $\mathbf{M}_0^e$ is the *baseline mass matrix*. This should be an acceptable mass matrix on its own if $\mu_1 = \ldots \mu_k = 0$. The simplest instance of (33.1) is a linear combination of the consistent and diagonally-lumped masss

$$\mathbf{M}^e \stackrel{\text{def}}{=} (1 - \mu)\mathbf{M}_C^e + \mu \mathbf{M}_L^e \tag{33.2}$$

This can be reformatted as (33.1) by writing $\mathbf{M}^e = \mathbf{M}_C^e + \mu(\mathbf{M}_L^e - \mathbf{M}_C^e)$. Here $k = 1$, the baseline is $\mathbf{M}_0^e \equiv \mathbf{M}_C^e$, $\mu \equiv \mu_1$ and $\mathbf{M}_1^e$ is the "consistent mass deviator" $\mathbf{M}_L^e - \mathbf{M}_C^e$. Expression (33.2) is often abbreviated to "LC-weighted mass matrix" or simply LCM.

A matrix-weighted mass template represents a tradeoff. It cuts down on the number of free parameters. Such a reduction is essential for 2D and 3D elements. It makes it easier to satisfy conservation and nonnegativity conditions through appropriate choice of the $\mathbf{M}_i^e$. On the minus side it generally spans only a subspace of acceptable matrices.

Spectral Parametrization. This has the form

$$\mathbf{M}^e \stackrel{\text{def}}{=} \mathbf{H}^T \mathbf{D}_\mu \mathbf{H}, \qquad \mathbf{D}_\mu = \mathbf{diag}\,[\, c_0\mu_0 \;\; c_1\mu_1 \;\; \ldots \;\; c_k\boldsymbol{\mu}_k \,]. \tag{33.3}$$

in which $\mathbf{H}$ is a generally full matrix. Parameters $\mu_0 \ldots \mu_k$ appear as entries of the diagonal matrix $\mathbf{D}_\mu$. Scaling coefficients c_i may be introduced for convenience. Often $\mu_0 = 1$ or $\mu_0 = 0$ are preset from conservation conditions.

Configuration (33.3) occurs naturally when the mass matrix is constructed first in generalized coordinates, followed by transformation to physical coordinates via $\mathbf{H}$. If the generalized mass is derived using mass-orthogonal functions (for example, Legendre polynomials in 1D elements), the unparametrized generalized mass $\mathbf{D} = \mathbf{diag}\,[\, c_0 \;\; c_1 \;\; \ldots c_k \,]$ is diagonal. Parametrization is effected by scaling entries of this matrix. Some entries may be left fixed, however, to satisfy *a priori* constraints.

Expanding (33.3) and collecting matrices that multiply μ_i leads to a matrix weighted combination form (33.1) in which each $\mathbf{M}_i^e$ is a rank-one matrix. The analogy with the spectral representation theorem of symmetric matrices is obvious. But in practice it is usually better to work directly with the congruent representation (33.3).

Entry-Weighted Parametrization. An entry-weighted mass template applies parameters directly to every entry of the mass matrix, except for *a priori* constraints on symmetry, invariance and

conservation. This form is the most general one and can be expected to lead to best possible solutions. But it is restricted to simple (usually 1D) elements because the number of parameters grows quadratically in the matrix size, whereas for the other two schemes it grows linearly.

Combined Approach. A hierarchical combination of parametrization schemes can be used to advantage if the kinetic energy can be naturally decomposed from physics. For example the Timoshenko beam element covered in Section 6 uses a two-matrix-weighted template form similar to (33.2) as top level. The two components are constructed by spectral and entry-weighted parametrization, respectively.

§33.4. Two-Node Bar Element

The template concept is best grasped through an example that involves the simplest structural finite element: the two-node prismatic bar of density ρ, area A and length ℓ, moving along x. See Figure 33.1. The most general form of the 2×2 mass matrix form is the entry-weighted template

FIGURE 33.1. The two-node prismatic bar element.

$$\mathbf{M}^e = \begin{bmatrix} M^e_{11} & M^e_{12} \\ M^e_{21} & M^e_{22} \end{bmatrix} = M^e \begin{bmatrix} \mu_{11} & \mu_{12} \\ \mu_{21} & \mu_{22} \end{bmatrix} = \rho A \ell \begin{bmatrix} \mu_{11} & \mu_{12} \\ \mu_{21} & \mu_{22} \end{bmatrix}. \tag{33.4}$$

The first form is merely a list of entries. To parametrize it, the total element mass $M^e = \rho A \ell$ is taken out as factor. The free parameters μ_{11} through μ_{22} are simply numbers. This illustrates a basic convenience rule: *free template parameters should be dimensionless*.

To cut down on the number of free parameters one looks at *mass property constraints*. The most common ones are

Matrix symmetry: $\mathbf{M}^e = (\mathbf{M}^e)^T$. For (33.4) this requires $\mu_{21} = \mu_{12}$.

Physical symmetry: For a prismatic bar $\mathbf{M}^e$ must exhibit antidiagonal symmetry: $\mu_{22} = \mu_{11}$.

Conservation of total translational mass: same as conservation of linear momentum or of kinetic energy. Apply the uniform velocity field $\dot{u} = v$ to the bar. The associated nodal velocity vector is $\dot{\mathbf{u}}^e = \mathbf{v}^e = v [\, 1 \; 1 \,]^T$. The kinetic energy is $T^e = \frac{1}{2}(\mathbf{v}^e)^T \mathbf{M}^e \mathbf{v}^e = \frac{1}{2} M^e v^2 (\mu_{11} + \mu_{12} + \mu_{21} + \mu_{22})$. This must equal $\frac{1}{2} M^e v^2$, whence $\mu_{11} + \mu_{12} + \mu_{21} + \mu_{22} = 1$.

Nonnegativity: $\mathbf{M}^e$ should not be indefinite. [This is not an absolute must, and it is actually relaxed in the Timoshenko beam element discussed in 33.6.] Whether checked by computing eigenvalues or principal minors, this constraint is nonlinear and of inequality type. Consequently it is not often applied *ab initio*, unless the element is quite simple, as in this case.

On applying the symmetry and conservation rules three parameters of (33.4) are eliminated. The remaining one, called μ, is taken for convenience to be $\mu_{11} = \mu_{22} = \frac{1}{6}(2 + \mu)$ and $\mu_{12} = \mu_{21} = \frac{1}{6}(1 - \mu)$, which gives

$$\begin{aligned} \mathbf{M}^e_\mu &= \tfrac{1}{6}\rho A \ell \begin{bmatrix} 2 + \mu & 1 - \mu \\ 1 - \mu & 2 + \mu \end{bmatrix} = (1 - \mu)\tfrac{1}{6}\rho A \ell \begin{bmatrix} 2 & 1 \\ 1 & 2 \end{bmatrix} + \mu \tfrac{1}{2}\rho A \ell \begin{bmatrix} 1 & 0 \\ 0 & 1 \end{bmatrix} \\ &= (1 - \mu)\mathbf{M}^e_C + \mu \mathbf{M}^e_L. \end{aligned} \tag{33.5}$$
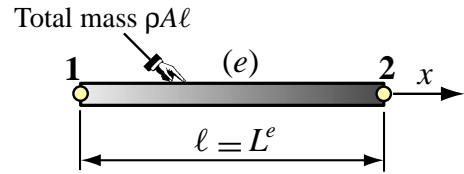
Expression (33.5) shows that the one-parameter template can be presented as a linear combination of the well known consistent and diagonally-lumped mass matrices. So starting with the general entry-weighted form (33.4) we end up with a two-matrix-weighted form befitting (33.2). If $\mu = 0$ and $\mu = 1$, (33.5) reduces to $\mathbf{M}_C^e$ and $\mathbf{M}_L^e$ respectively. This illustrates another desirable property: the CMM and DLMM models ought to be instances of the template.

Finally we can apply the nonnegativity constraint. For the two principal minors of $\mathbf{M}_\mu^e$ to be nonnegative, $2 + \mu \geq 0$ and $(2 + \mu)^2 - (1 - \mu)^2 = 3 + 6\mu \geq 0$. Both are satisfied if $\mu \geq -1/2$. Unlike the others, this constraint is of inequality type, and only limits the range of μ.

The remaining task is to find μ. This is done by introducing an *optimality criterion that fits the problem at hand*. This is where customization comes in. Even for this simple case the answer is not unique. Thus the sentence "the best mass matrix for the two-node bar is so-and-so" has no unique meaning. Two specific optimization criteria are studied below.

§33.4.1. Best μ by Angular Momentum Preservation

Allow the bar to move in the $\{x, y\}$ plane by expanding its nodal DOF to $\mathbf{u}^e = [\, u_{x1} \; u_{y1} \; u_{x2} \; u_{y2} \,]^T$ so (33.5) becomes a 4×4 matrix

$$
\mathbf{M}_\mu^e = \tfrac{1}{6}\rho A \ell \begin{bmatrix} 2 + \mu & 0 & 1 - \mu & 0 \\ 0 & 2 + \mu & 0 & 1 - \mu \\ 1 - \mu & 0 & 2 + \mu & 0 \\ 0 & 1 - \mu & 0 & 2 + \mu \end{bmatrix} \tag{33.6}
$$

Apply a uniform angular velocity $\dot{\theta}$ about the midpoint. The associated node velocity vector at $\theta = 0$ is $\dot{\mathbf{u}}^e = \tfrac{1}{2}\ell\dot{\theta}\,[\, 0 \; -1 \; 0 \; 1 \,]^T$. The discrete and continuum energies are

$$
T_\mu^e = \tfrac{1}{2}(\dot{\mathbf{u}}^e)^T \mathbf{M}_\mu^e \dot{\mathbf{u}}^e = \tfrac{1}{24}\rho A\ell^3(1 + 2\mu), \quad T^e = \int_{-\ell/2}^{\ell/2} \rho A(\dot{\theta}\,x)^2 \, dx = \tfrac{1}{24}\rho A\ell^3. \tag{33.7}
$$

Matching $T_\mu^e = T^e$ gives $\mu = 0$. So according to this criterion the optimal mass matrix is the consistent one (CMM). Note that if $\mu = 1$, $T_\mu^e = 3T^e$, whence the DLMM overestimates the rotational (rotary) inertia by a factor or 3.

§33.4.2. Best μ by Fourier Analysis

Another useful optimization criterion is the fidelity with which planes waves are propagated over a bar element lattice, when compared to the case of a continuum bar pictured in Figure 33.2.

Symbols used for propagation of harmonic waves are collected in Table 33.1 for the reader's convenience. (Several of these are reused in Sections 5 and 6.) The discrete counterpart of Figure 33.2 is shown in Figure 33.3.
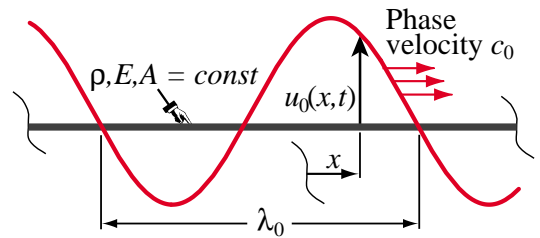

FIGURE 33.2. Propagation of a harmonic wave over an infinite, continuum prismatic bar. The wave-profile axial displacement $u(x, t)$ is plotted normal to the bar.

This is a lattice of repeating two-node bar elements of length ℓ. Lattice wave propagation nomenclature is similar to that defined for the continuum case in Table 33.1, but without zero subscripts.

Table 33.1   Nomenclature for Harmonic Wave Propagation in a Continuum Bar

Quantity	Meaning (physical dimension in brackets)
ρ, E, A	Mass density, elastic modulus, and cross section area of bar
$\rho \ddot{u}_0 = E u_0''$	Bar wave equation. Alternate forms: $-\omega_0^2 u = c_0^2 u''$ and $u'' + k_0^2 u = 0$.
$u_0(x, t)$	Waveform $u_0 = B_0 \exp\big(i(k_0 x - \omega_0 t)\big)$ [length], in which $i = \sqrt{-1}$
B_0	Wave amplitude [length]
λ_0	Wavelength [length]
k_0	Wavenumber $k_0 = 2\pi/\lambda_0$ [1/length]
ω_0	Circular (a.k.a. angular) frequency $\omega_0 = k_0 c_0 = 2\pi f_0 = 2\pi c_0/\lambda_0$ [radians/time]
f_0	Cyclic frequency $f_0 = \omega_0/(2\pi)$ [cycles/time: Hz if time in seconds]
T_0	Period $T_0 = 1/f_0 = 2\pi/\omega_0 = \lambda_0/c_0$ [time]
c_0	Phase velocity $c_0 = \omega_0/k_0 = \lambda_0/T_0 = \lambda_0 f_0 = \sqrt{E/\rho}$ [length/time]
κ_0	Dimensionless wavenumber $\kappa_0 = k_0\lambda_0$ ($\kappa_0 = 2\pi$ in continuum)
Ω_0	Dimensionless circular frequency $\Omega_0 = \omega_0 T_0 = \omega_0\lambda_0/c_0$

Zero subscripted quantities, such as k_0 or c_0, refer to the continuum bar. Unsubscripted counterparts, such as k or c, pertain to a discrete FEM lattice as in Figure 33.3.

The lattice propagation process is governed by the semidiscrete equation of motion $\mathbf{M}\ddot{\mathbf{u}} + \mathbf{K}\mathbf{u} = \mathbf{0}$, which can be solved by Fourier methods. To study solutions it is sufficient to extract a two-element patch as illustrated in Figure 33.3(a). Within some constraints noted later the lattice can propagate travelling harmonic waves of wavelength λ and phase velocity c, as depicted in Figure 33.3(b). The wavenumber is $k = 2\pi/\lambda$ and the circular frequency $\omega = 2\pi/T = 2\pi c/\lambda = kc$. Figure 33.3(b) displays two characteristic lengths: λ and ℓ. The element-to-wavelength ratio is called $\chi = \ell/\lambda$. This ratio characterizes the fineness of the discretization with respect to wavelength. A harmonic wave of amplitude B is described by the function

$$u(x, t) = B \exp[i(kx - \omega t)] = B \exp\big[i(\kappa x - \Omega c_0 t)/\ell\big], \quad i = \sqrt{-1}. \qquad (33.8)$$

Here the dimensionless wavenumber κ and circular frequency Ω are defined as $\kappa = k\ell = 2\pi\ell/\lambda = 2\pi\chi$ and $\Omega = \omega\ell/c_0$, respectively, in which $c_0 = \sqrt{E/\rho}$ is the continuum bar wavespeed. Using the well-known bar stiffness matrix and the mass template (33.5) gives the patch equations

$$\frac{\rho A \ell}{6} \begin{bmatrix} 2+\mu & 1-\mu & 0 \\ 1-\mu & 4+2\mu & 1-\mu \\ 0 & 1-\mu & 2+\mu \end{bmatrix} \begin{bmatrix} \ddot{u}_{j-1} \\ \ddot{u}_j \\ \ddot{u}_{j+1} \end{bmatrix} + \frac{EA}{\ell} \begin{bmatrix} 1 & -1 & 0 \\ -1 & 2 & -1 \\ 0 & -1 & 1 \end{bmatrix} \begin{bmatrix} u_{j-1} \\ u_j \\ u_{j+1} \end{bmatrix} = 0. \qquad (33.9)$$

From this one takes the middle (node j) equation, which repeats in the infinite lattice:

$$\frac{\rho A \ell}{6} \begin{bmatrix} 1-\mu & 4+2\mu & 1-\mu \end{bmatrix} \begin{bmatrix} \ddot{u}_{j-1} \\ \ddot{u}_j \\ \ddot{u}_{j+1} \end{bmatrix} + \frac{EA}{\ell} \begin{bmatrix} -1 & 2 & -1 \end{bmatrix} \begin{bmatrix} u_{j-1} \\ u_j \\ u_{j+1} \end{bmatrix} = 0. \qquad (33.10)$$

Evaluate (33.8) at $x = x_{j-1} = x_j - \ell$, $x = x_j$ and $x = x_{j+1} = x_j + \ell$ while keeping t continuous. Substitution into (33.10) gives the wave propagation condition

$$\frac{\rho A c_0^2}{3\ell}\Big[6 - (2+\mu)\Omega^2 - \big(6 - (1-\mu)\Omega^2\big)\cos\kappa\Big]\left(\cos\frac{\Omega c_0 t}{\ell} - i\sin\frac{\Omega c_0 t}{\ell}\right) B = 0. \qquad (33.11)$$
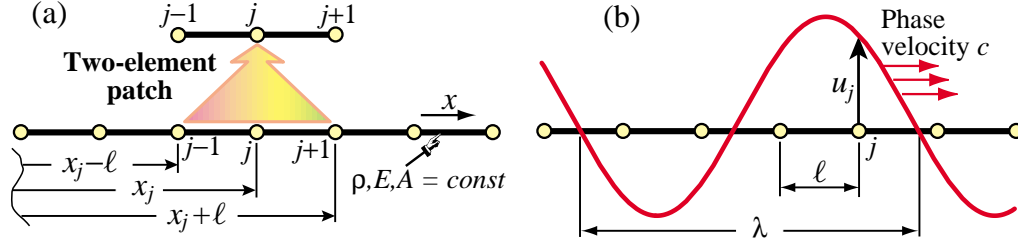
FIGURE 33.3. An infinite lattice of two-node prismatic bar elements: (a) 2-element patch extracted from lattice; (b) characteristic dimensions for a propagating harmonic wave.

If this is to be zero for any t and B, the expression in brackets must vanish. Solving gives the frequency-wavenumber relations

$$
\Omega^2 = \frac{6(1 - \cos \kappa)}{2 + \mu + (1 - \mu) \cos \kappa} = \kappa^2 + \frac{1 - 2\mu}{12} \kappa^4 + \frac{1 - 10\mu + 10\mu^2}{360} \kappa^6 + \ldots,
$$

$$
\kappa = \arccos \left[\frac{6 - (2 + \mu)\Omega^2}{6 + (1 - \mu)\Omega^2} \right] = \Omega - \frac{1 - 2\mu}{24} \Omega^3 + \frac{9 - 20\mu + 20\mu^2}{1920} \Omega^5 + \ldots
$$

(33.12)

Returning to physical wavenumber $k = \kappa/\ell$ and frequency $\omega = \Omega c_0/\ell$:

$$
\omega^2 = \left(\frac{6c_0^2}{\ell^2} \right) \frac{1 - \cos(k\ell)}{2 + \mu + (1 - \mu) \cos(k\ell)} = c_0^2 k^2 \left(1 + \frac{1 - 2\mu}{12} k^2 \ell^2 + \frac{1 - 10\mu + 10\mu^2}{360} k^4 \ell^4 + \ldots \right)
$$

(33.13)

An equation that links frequency and wavenumber: $\omega = \omega(k)$ as in (33.13), is a *dispersion relation*. An oscillatory dynamical system is *nondispersive* if ω is linear in k, in which case $c = \omega/k$ is constant and the wavespeed is the same for all frequencies. The dispersion relation for the continuum bar (within the limits of MoM assumptions) is $c_0 = \omega_0/k_0$: all waves propagate with the same speed c_0. On the other hand the FEM model is *dispersive* for any μ, since from (33.12) we get

$$
\frac{c}{c_0} = \frac{\omega}{k c_0} = \frac{1}{\kappa} \sqrt{\frac{6(1 - \cos \kappa)}{2 + \mu + (1 - \mu) \cos \kappa}} = 1 + \frac{1 - 2\mu}{24} \kappa^2 + \frac{1 - 20\mu + 20\mu^2}{1920} \kappa^4 + \ldots \quad (33.14)
$$

The best fit to the continuum for *small wavenumbers* $\kappa = k\ell << 1$ is obtained by taking $\mu = 1/2$. This makes the second term of the foregoing series vanish. So from this standpoint the best mass matrix for the bar is

$$
\mathbf{M}^e_\mu \big|_{\mu=1/2} = \tfrac{1}{2}\mathbf{M}^e_C + \tfrac{1}{2}\mathbf{M}^e_L = \frac{\rho A \ell}{12} \begin{bmatrix} 5 & 1 \\ 1 & 5 \end{bmatrix}.
$$

(33.15)

Figure 33.4(a) plots the dimensionless dispersion relation (33.12) for the consistent ($\mu = 0$), diagonally lumped ($\mu = 1$) and LC-averaged ($\mu = 1/2$) mass matrices, along with the continuum-bar relation $\Omega_0 = \kappa_0$. The lattice curves of Figure 33.4(a) have a 2π period: $\Omega(\kappa) = \Omega(\kappa + 2\pi n)$, n being an integer. Thus it is enough to plot $\Omega(\kappa)$ over $\kappa \in [0, 2\pi]$. The maximum lattice frequency, which occurs for $\kappa = k\ell = \pi$ or $\lambda = 2\ell$, is called the *Nyquist* or *folding frequency*.

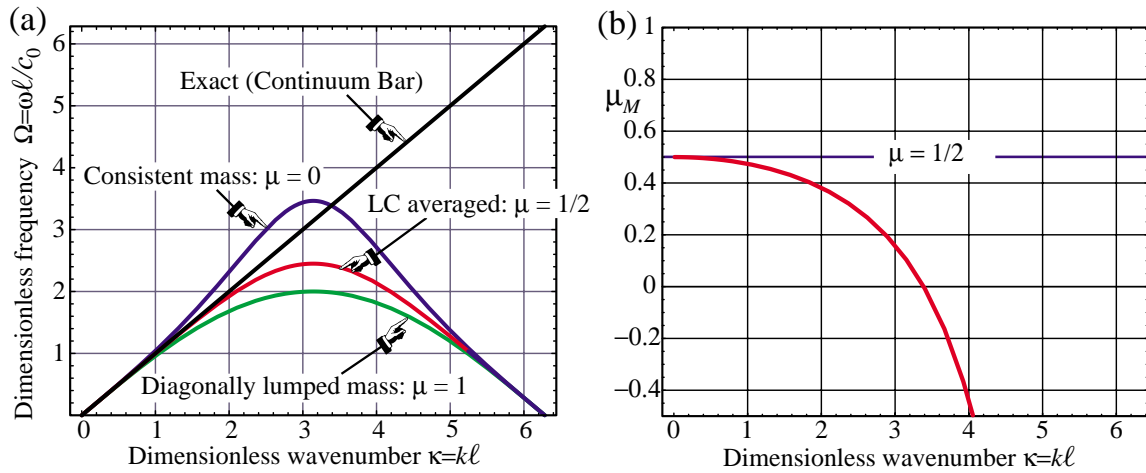If it is possible to pick μ as function of Ω or κ we can match the continuum over a certain range of

FIGURE 33.4. Results from Fourier analysis of two-node bar lattice: (a) dispersion curves for various choices of μ; (b) wavenumber dependent μ_M that makes lattice match the continuum.

κ or Ω. This can be done by equating $\Omega = \kappa$ (or $c = c_0$) and solving for μ:

$$\mu_M = 1 + \frac{6}{\kappa^2} - \frac{3}{1-\cos\kappa} = \frac{1}{2} - \frac{\kappa^2}{40} - \frac{\kappa^4}{1008} - \frac{\kappa^6}{28800} - \cdots = \frac{1}{2} - \frac{4\pi^2\chi^2}{40} - \frac{16\pi^4\chi^4}{1008} - \cdots$$

$$= 1 + \frac{6}{\Omega^2} - \frac{3}{1-\cos\Omega} = \frac{1}{2} - \frac{\Omega^2}{40} - \frac{\Omega^4}{1008} - \frac{\Omega^6}{28800} - \cdots$$

(33.16)

in which $\chi = 2\pi\kappa$. The function $\mu_M(\kappa)$ is plotted in Figure 33.4(b). Interesting values are $\mu_M = 0$ if $\kappa = 3.38742306673364$ and $\mu_M = -1/2$ if $\kappa = \kappa_{lim} = 4.05751567622863$. If $\kappa > \kappa_{lim}$ the fitted $\mathbf{M}^e$ becomes indefinite. So (33.16) is practically limited to the range $0 \le k \le \approx 4/\ell$ shown in the plot.

§33.4.3. *Best μ By Modified Equation

The gist of Fourier analysis is to find an exact solution, which separates space and time in the characteristic equation (33.11). The rest is routine mathematics. The method of modified differential equations or MoDE, introduced in §13.8, makes less initial assumptions but is not by any means routine. The objective is to find a MoDE that, if solved exactly, produces the FEM solution at nodes, and to compare it with the continuum wave equation given in Table 33.1. The method assumes only[1] that $\ddot{\mathbf{u}} = -\omega^2\mathbf{u}$, where ω is a lattice frequency left to be determined. This takes care of the time variation. Applying this assumption to the patch equation (33.10) and passing to dimensionless variables we get

$$\left[-1 - \tfrac{1}{6}(1-\mu)\Omega^2 \quad 2 - \tfrac{1}{6}(4+2\mu)\Omega^2 \quad -1 - \tfrac{1}{6}(1-\mu)\Omega^2 \right] \begin{bmatrix} u_{j-1} \\ u_j \\ u_{j+1} \end{bmatrix} = 0. \qquad (33.17)$$

---

[1] This assumption is necessary because no discretization in the time domain has been specified. If a time integrator had been applied, we would face a partial differential equation in space and time. That is a tougher nut to crack in an introductory course.

in which $\Omega = \omega\ell/c_0$ is the dimensionless circular frequency used in the previous subsection. This difference equation is "continuified" by replacing $u_j \to u(t)$ and $u_{j\pm1} \to u(t \pm \ell)$, and scaled through to produce the following difference-differential form or DDMoDE:

$$[-\tfrac{1}{2} \quad \psi \quad -\tfrac{1}{2}] \begin{bmatrix} u(t-\ell) \\ u(t) \\ u(t+\ell) \end{bmatrix} = \psi u(t) - \tfrac{1}{2}\big(u(t-\ell)+u(t+\ell)\big) = 0, \quad \text{with } \psi = \frac{6-(2+\mu)\Omega^2}{6+(1-\mu)\Omega^2}. \quad (33.18)$$

As MoDE expansion coefficient we select the element-to-wavelength ratio $\chi = \ell/\lambda$. Accordingly, expanding the the end values in Taylor series about $u(t)$ gives $u(t-\ell) = u_j - \ell u'(t) + \ell^2 u''(t)/2! - \ldots$, and $u(t+\ell) = u_j + \ell u'(t) + \ell^2 u''(t)/2! + \ldots$. The foregoing semisum is $\tfrac{1}{2}\big(u(t-\ell)+u(t+\ell)\big) = u(t) + \ell^2 u''(t)/2! + \ell^4 u''''(t)/4! + \ldots$, which contains only even u derivatives. Replacing into (33.18) and setting $\ell = \lambda\chi$, we obtain the infinite-order modified differential equation or IOMoDE:

$$(1-\psi)u + \frac{1}{2!}\lambda^2\chi^2 u'' + \frac{\lambda^4\chi^4}{4!}u'''' + \ldots = 0. \quad (33.19)$$

This form needs further work. To see why, consider a mesh refinement process that makes $\chi \to 0$ while keeping λ fixed. Then (33.19) approaches $(1-\psi)u = 0$. Since $u \neq 0$, $\psi \to 1$ in the sense that $1-\psi = O(\chi^2)$. To obtain the canonical MoDE form exhibited below, the transformation $1-\psi \to \tfrac{1}{2}\gamma\chi^2$, where γ is another free coefficient, is specified, and solved for Ω^2, giving $\Omega^2 = 6\gamma\chi^2/(6 - \gamma(1-\mu)\chi^2)$. Replacing into (33.19)and dividing through by $\ell^2 = \lambda^2\chi^2$ yields

$$\frac{\gamma}{2\lambda^2}u + \frac{1}{2!}u'' + \frac{\lambda^2\chi^2}{4!}u'''' + \frac{\lambda^4\chi^4}{6!}u'''''' + \ldots = 0. \quad (33.20)$$

This has the correct IOMoDE form: as $\chi - > 0$ two terms survive and a second-order ODE emerges. In fact, but for the sign of the first term this is a canonical IOMoDE form studied in [94] for a different application. The last and quite complicated MoDE step is elimination of derivatives of order higher than two. The technique of that reference leads to the finite order modified equation or FOMoDE:

$$u'' + \frac{4}{\lambda^2\chi^2}\left(\arcsin\frac{\chi\sqrt{\gamma}}{2}\right)^2 u = 0. \quad (33.21)$$

This is matched to the continuum bar equation $u'' + k_0^2 u = 0$ of Table 33.1, assuming that $\lambda = \lambda_0$. Equating coefficients gives $k_0\lambda_0\chi/2 = \pi\chi = \arcsin(\tfrac{1}{2}\chi\sqrt{\gamma})$ or $\sin(\pi\chi) = \tfrac{1}{2}\chi\sqrt{\gamma}$, whence $\gamma = 4\sin^2(\pi\chi)/\chi^2$ and

$$\Omega^2 = \frac{6\gamma\chi^2}{6-\gamma(1-\mu)\chi^2} = \frac{12\sin^2(\pi\chi)}{2+\mu+(1-\mu)\cos(2\pi\chi)} = 4\pi^2\chi^2. \quad (33.22)$$

The last equation comes from the definition $\Omega = \omega\ell/c_0 = 2\pi\chi$. Solving for μ gives the discrete-to-continuum matching value

$$\mu_M = 1 + \frac{3}{2\pi^2\chi^2} - \frac{3}{2\cos^2(\pi\chi)} = \frac{1}{2} - \frac{\pi^2\chi^2}{10} - \frac{\pi^4\chi^4}{63} - \frac{\pi^6\chi^6}{450} - \ldots \quad (33.23)$$

Replacing $2\pi\chi$ by κ (or by $\Omega = \kappa$) gives $\mu_M = 1 + 6/\kappa^2 - 3/(1-\cos\kappa)$, thus reproducing the result (33.16). So Fourier analysis and MoDE deliver the same result.

Remark 33.1. When Fourier can be used, as here, it is far simpler than MoDE. However the latter provides a side bonus: *a priori* error estimates. For example, suppose that one plans to put 10 elements within the shortest wavelength of interest. Thus $\chi = \ell/\lambda = 1/10$ and $\gamma = 4\sin^2(\pi\chi)/\chi^2 = 38.1966$. Replacing into (33.22) gives $\Omega/(2\pi\chi) = 1.016520, 0.999670$ and 0.983632 for $\mu = 0$, $\mu = \tfrac{1}{2}$ and $\mu = 1$, respectively. The estimate frequency errors with respect to the continuum are 1.65%, -0.04% and -1.64%, respectively.

§33.5. Three-Node Bar Element

As pictured in Figure 33.5, this element is prismatic with length ℓ, cross section area A and mass density ρ. Midnode 3 is at the center. The element DOFs are arranged as $\mathbf{u}^e = [\, u_1 \;\; u_2 \;\; u_3 \,]^T$. Its well known stiffness matrix is paired with a entry-weighted mass template:
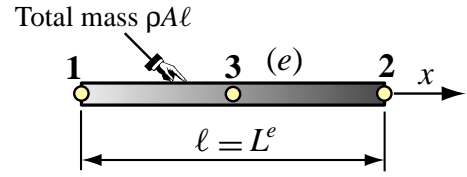
Total mass $\rho A\ell$

FIGURE 33.5. The three-node prismatic bar element.

$$\mathbf{K}^e = \frac{EA}{3\ell}\begin{bmatrix} 7 & 1 & -8 \\ 1 & 7 & -8 \\ -8 & -8 & 16 \end{bmatrix}, \quad \mathbf{M}^e_\mu = \frac{\rho A\ell}{90}\begin{bmatrix} 12+\mu_1 & -3+\mu_3 & 6+\mu_4 \\ -3+\mu_3 & 12+\mu_1 & 6+\mu_4 \\ 6+\mu_4 & 6+\mu_4 & 48+\mu_2 \end{bmatrix} \quad (33.24)$$

The idea behind the assumed form of $\mathbf{M}^e_\mu$ in (33.24) is to define the mass template as a parametrized deviation from the consistent mass matrix. That is, setting $\mu_1 = \mu_2 = \mu_3 = \mu_4 = 0$ makes $\mathbf{M}^e_\mu = \mathbf{M}^e_C$. Setting $\mu_1 = \mu_3 = 3$, $\mu_2 = 12$ and $\mu_4 = -6$ gives the well known diagonally lumped mass matrix (DLMM) generated by Simpson's integration rule: $\mathbf{M}^e_L = \rho A\,\ell\,\mathbf{diag}\left[\,1/6,\; 1/6,\; 2/3\,\right]$. Thus again the standard models are template instances. Notice that $\mathbf{M}^e_\mu$ in (33.24) incorporates matrix and physical symmetries *a priori* but not conservation conditions.

Linear and angular momentum conservation requires $2\mu_1 + \mu_2 + 2\mu_3 + 4\mu_4 = 0$ and $\mu_3 = \mu_1$, respectively. Eliminating μ_3 and μ_4 from those constraints reduces the template to two parameters:

$$\mathbf{M}^e_\mu = \frac{\rho A\ell}{360}\begin{bmatrix} 4(12+\mu_1) & 4(-3+\mu_1) & 24-4\mu_1-\mu_2 \\ 4(-3+\mu_1) & 4(12+\mu_1) & 24-4\mu_1-\mu_2 \\ 24-4\mu_1-\mu_2 & 24-4\mu_1-\mu_2 & 4(48+\mu_2) \end{bmatrix} \quad (33.25)$$

For (33.25) to be nonnegative, $\mu_1 \geq -9/2$ and $15 + \mu_1 - 3\sqrt{5}\sqrt{9+2\mu_1} \leq \frac{1}{4}\mu_2 \leq 15 + \mu_1 + 3\sqrt{5}\sqrt{9+2\mu_1}$. These inequality constraints should be checked *a posteriori*.
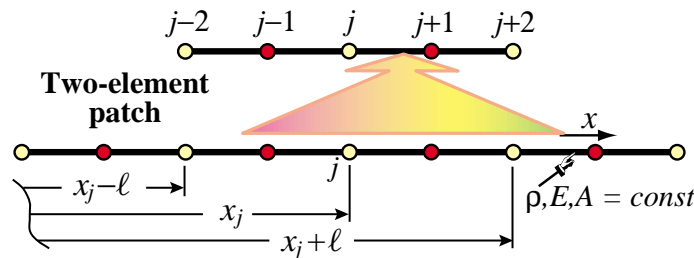

FIGURE 33.6. Lattice of three-node bar elements from which a 2-element patch is extracted. Yellow and red-filled circles flag endnodes and midnodes, respectively.

§**33.5.1. Patch Equations**

Unlike the two-node bar, two free parameters remain after the angular momentum conservation condition is enforced. Consequently we can ask for satisfactory wave propagation conditions in addition to conservation. To assess performance of mass-stiffness combinations we carry out the plane wave analysis of the infinite beam lattice shown in Figure 33.6.

From the lattice we extract a typical two node patch as illustrated. The patch has five nodes: three endpoints and two midpoints, which are assigned global numbers $j-2, j-1, \ldots j+2$. The unforced semidiscrete dynamical equations of the patch are $\mathbf{M}^P \ddot{\mathbf{u}}^P + \mathbf{K}^P \mathbf{u}^P = \mathbf{0}$, where

$$
\mathbf{M}^P = \frac{\rho A \ell}{360}
\begin{bmatrix}
4(12+\mu_1) & 24-4\mu_1-\mu_2 & 4(-3+\mu_1) & 0 & 0 \\
24-4\mu_1-\mu_2 & 4(48+\mu_2) & 24-4\mu_1-\mu_2 & 0 & 0 \\
4(-3+\mu_1) & 24-4\mu_1-\mu_2 & 8(12+\mu_1) & 24-4\mu_1-\mu_2 & 4(-3+\mu_1) \\
0 & 0 & 24-4\mu_1-\mu_2 & 4(48+\mu_2) & 24-4\mu_1-\mu_2 \\
0 & 0 & 4(-3+\mu_1) & 24-4\mu_1-\mu_2 & 4(12+\mu_1)
\end{bmatrix}
$$

$$
\mathbf{K}^P = \frac{EA}{3\ell}
\begin{bmatrix}
7 & -8 & 1 & 0 & 0 \\
-8 & 16 & -8 & 0 & 0 \\
1 & -8 & 14 & -8 & 1 \\
0 & 0 & -8 & 16 & -8 \\
0 & 0 & 1 & -8 & 7
\end{bmatrix}, \qquad
\mathbf{u}^P = [\, u_{j-2} \quad u_{j-1} \quad u_j \quad u_{j+1} \quad u_{j+2} \,]^T .
$$

$$\text{(33.26)}$$

From the foregoing we keep the third and fourth equations, namely those for nodes j and $j+1$. This selection provides the equations for a typical corner point j and a typical midpoint $j+1$. The retained patch equations are

$$
\mathbf{M}^P_{j,j+1} \ddot{\mathbf{u}}_P + \mathbf{K}^P_{j,j+1} \mathbf{u}_P = \mathbf{0}.
\tag{33.27}
$$

The 2×5 matrices $\mathbf{M}^P_{j,j+1}$ and $\mathbf{K}^P_{j,j+1}$ result on deleting rows 1,2,5 of $\mathbf{M}^P$ and $\mathbf{K}^P$, respectively.

§**33.5.2. Fourier Analysis**

We study the propagation of harmonic plane waves of wavelength λ, wavenumber $k = 2\pi/\lambda$, and circular frequency ω over the lattice of Figure 33.6. For convenience they are separated into corner and midpoint waves:

$$
u_c(x, t) = B_c\, e^{i(kx-\omega t)}, \qquad u_m(x, t) = B_m e^{i(kx-\omega t)}.
\tag{33.28}
$$

Wave $u_c(x, t)$ propagates only over corners and vanishes at midpoints, whereas $u_m(x, t)$ propagates only over midpoints and vanishes at corners. Both have the same wavenumber and frequency but different amplitudes and phases. [Waves (33.28) can be combined to form a single waveform that propagates over all nodes. The combination has two components that propagate with the same speed but in opposite directions. This is useful when studying boundary conditions or transitions in finite lattices, but is not needed for a periodic infinite lattice.] As in the two-node bar case, we will work with the dimensionless frequency $\Omega = \omega\ell/c_0$ and dimensionless wavenumber $\kappa = k\ell$.

Inserting (33.28) into (33.26), passing to dimensionless variables and requiring that solutions exist for any t yields the characteristic equation

$$\frac{1}{180}\begin{bmatrix} 960 - 2(48 + \mu_2)\Omega^2 & -\big(960 + (24 - 4\mu_1 - \mu_2)\Omega^2\big)\cos\tfrac{1}{2}\kappa \\ \text{symm} & 4\big(210 - (12+\mu_1)\Omega^2 + (30 + (3-\mu_1)\Omega^2)\cos\kappa\big) \end{bmatrix}\begin{bmatrix} B_c \\ B_m \end{bmatrix} = \mathbf{0}.$$
(33.29)

For nontrivial solutions the determinant of the characteristic matrix must vanish. Solving for Ω^2 gives two frequencies for each wavenumber κ. They can be expressed as the dispersion relations

$$\Omega_a^2 = \frac{\phi_1 + \delta}{\phi_5 + \phi_6 \cos\kappa}, \qquad \Omega_o^2 = \frac{\phi_1 - \delta}{\phi_5 + \phi_6 \cos\kappa}, \tag{33.30}$$

in which $\phi_1 = 720(-208 - \mu_2 + (\mu_2 - 32)\cos\kappa)$, $\phi_2 = 64(\mu_1 - 60)\mu_1 - 32\mu_1\mu_2 + 13\mu_2^2 + 384(474 + \mu_2)$, $\phi_3 = 12(-112 + \mu_2)(128 + \mu_2)$, $\phi_4 = 64(132 + (\mu_1 - 60)\mu_1) - 32(\mu_1 - 6)\mu_2 + \mu_2^2$, $\phi_5 = 16(-540 + (\mu_1 - 60)\mu_1) - 8(30 + \mu_1)\mu_2 + \mu_2^2$, $\phi_6 = 2880 + 16(\mu_1 - 60)\mu_1 - 8\mu_1\mu_2 + \mu_2^2$ and $\delta = 120\sqrt{6}\sqrt{\phi_2 - \phi_3\cos\kappa - \phi_4\cos 2\kappa}$. Frequencies Ω_a and Ω_o pertain to the so-called *acoustic* and *optical* branches, respectively. This nomenclature originated in crystal physics, in which both branches have physical meaning as modeling molecular oscillations. [In molecular crystallography, acoustic waves are long-wavelength, low-frequency mechanical waves caused by sonic-like disturbances, in which adjacent molecules move in the same direction. Optical waves are short-wavelength, high-frequency oscillations caused by interaction with light or electromagnetics, in which adjacent molecules move in opposite directions. **Notes and Bibliography** provides references.]

Figure 33.7 illustrates nomenclature used for a two-branched dispersion diagram such as that given by (33.30). The meaning of terms such as "stopping band" is defined below. In FEM discretization work only the acoustic branch has physical meaning because for small κ (that is, long wavelengths) it approaches the continuum bar relation $\Omega = \kappa$, as shown below in (33.31). On the other hand, the optical branch is physically spurious. It is caused by the discretization and pertains to high-frequency lattice oscillations, also known as "mesh modes."
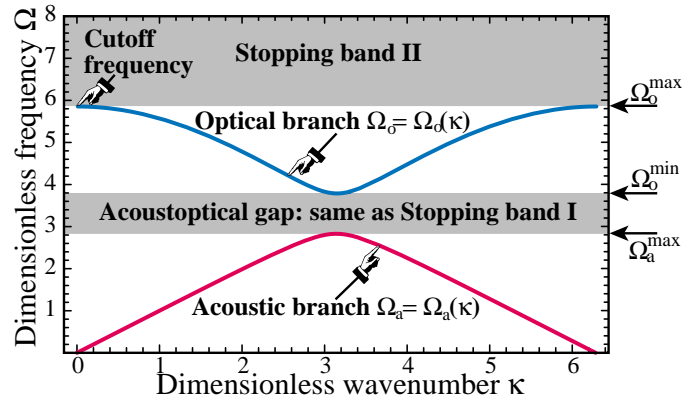
FIGURE 33.7. Notation pertaining to a typical two-branch dispersion diagram. The stopping band is the union of I and II.

The distinction between the two branches can be better grasped by examining the Taylor expansions of the frequencies (33.30) about $\kappa = 0$:

$$\Omega_a^2 = \kappa^2 + \frac{C_4\kappa^4}{4!} + \frac{C_6\kappa^6}{6!} + \frac{C_8\kappa^8}{8!} + \dots, \qquad \Omega_o^2 = D_0 + \frac{D_2\kappa^2}{2!} + \dots, \tag{33.31}$$

in which

$$5 \times 1440\, C_4 = 14400 - \psi_1^2 = (240 - 4\mu_1 + \mu_2)(4\mu_1 - \mu_2),$$

$$10 \times 1440^2\, C_6 = 41472000 + 7200\psi_1^2 + 180\psi_1^3 + \psi_1^4 - 720\psi_1^2\psi_2,$$

$$60 \times 1440^3\, C_8 = -2030469120000 + 348364800\psi_1^2 - 14515200\psi_1^3 - 342720\psi_1^4 - 2520\psi_1^5$$

$$- 7\psi_1^6 + 58060800\psi_1^2\psi_2 + 1451520\psi_1^3\psi_2 + 10080\psi_1^4\psi_2 - 2903040\psi_1^2\psi_2^2, \tag{33.32}$$

$$D_0 = \frac{1}{\psi_3}, \quad D_2 = -\frac{\psi_1^2(43200 + 360\psi_1 + \psi_1^2 - 1440\psi_2)}{\psi_3^2}.$$

Here $\psi_1 = 4\mu_1 - \mu_2 - 120$, $\psi_2 = \mu_1 - 2$ and $\psi_3 = 28800 + 360\psi_1 + \psi_1^2 - 1440\psi_2 = -2880 - 960\mu_1 + 16\mu_1^2 - 120\mu_2 - 8\mu_1\mu_2 + \mu_2^2$. Note that the expansion of Ω_a^2 approaches κ^2 as $\kappa \to 0$. Clearly the acoustic branch is the long-wavelength counterpart of the continuum bar, for which $\Omega = \kappa$. On the other hand, the optical branch has a nonzero frequency $\Omega_o^2 = 1/\psi_3$ at $\kappa = 0$, called the *cutoff frequency*, which cannot vanish although it may go to infinity if $\psi_3 = 0$. As illustrated in Figure 33.7, the lowest and highest values of Ω_o (taking the $+$ square root of Ω_o^2) are called Ω_o^{max} and Ω_o^{min}, respectively, while the largest Ω_a is called Ω_a^{max}. Usually, but not always, Ω_0^{min} and Ω_a^{max} occur at $\kappa = \pi$.

If $\Omega_o^{min} > \Omega_a^{max}$, the range $\Omega_o^{min} > \Omega > \Omega_a^{max}$ is called the *acoustoptical frequency gap* or simply the AO gap. Frequencies in this gap are said to pertain to portion I of the *stopping band*, a term derived from filter technology. Frequencies $\Omega > \Omega_o^{max}$ pertain to portion II of the stopping band. A stopping band frequency cannot be propagated as harmonic plane wave over the lattice. This can be proven by showing that if Ω pertains to the stopping band, the characteristic equation (33.29) has complex roots with nonzero real parts. This causes exponential attenuation so any disturbance with that frequency will decay exponentially.

Table 33.2. Useful Mass Matrices for Three-Node Bar Element

Mass matrix	Template signature μ_1 μ_2 μ_3 μ_4				Taylor expansion of Ω_a^2 (acoustic branch)	Taylor expansion of Ω_o^2 (optical branch)
CMM	0	0	0	0	$\kappa^2 + \frac{\kappa^6}{720} - \frac{11\kappa^8}{151200} + \frac{7\kappa^{10}}{129600} + O(\kappa^{12})$	$60 - 20\kappa^2 + O(\kappa^4)$
DLMM	3	12	3	−6	$\kappa^2 - \frac{\kappa^6}{1440} - \frac{\kappa^8}{48383} - \frac{\kappa^{10}}{4147200} + O(\kappa^{12})$	$24 - 2\kappa^2 + O(\kappa^4)$
BLC	2	8	2	−4	$\kappa^2 - \frac{\kappa^8}{37800} - \frac{\kappa^{10}}{864000} + O(\kappa^{12})$	$30 - \frac{15\kappa^2}{4} + O(\kappa^4)$
COF	8	32	8	−16	$\kappa^2 - \frac{\kappa^6}{240} - \frac{\kappa^8}{6048} + \frac{\kappa^{10}}{86400} + O(\kappa^{12})$	12

§33.5.3. Customization

Figure 33.8 shows dispersion curves for the four parameter settings tabulated in Table 33.2. The four associated mass matrices are positive definite. Dispersion curves for the consistent mass $\mathbf{M}_C^e$ and the diagonally lumped mass $\mathbf{M}_L^e$ are shown in (a,b). Both matrices have an acoustical branch that agrees with the continuum to order $O(\kappa^4)$, as shown by the series listed in Table 33.2.
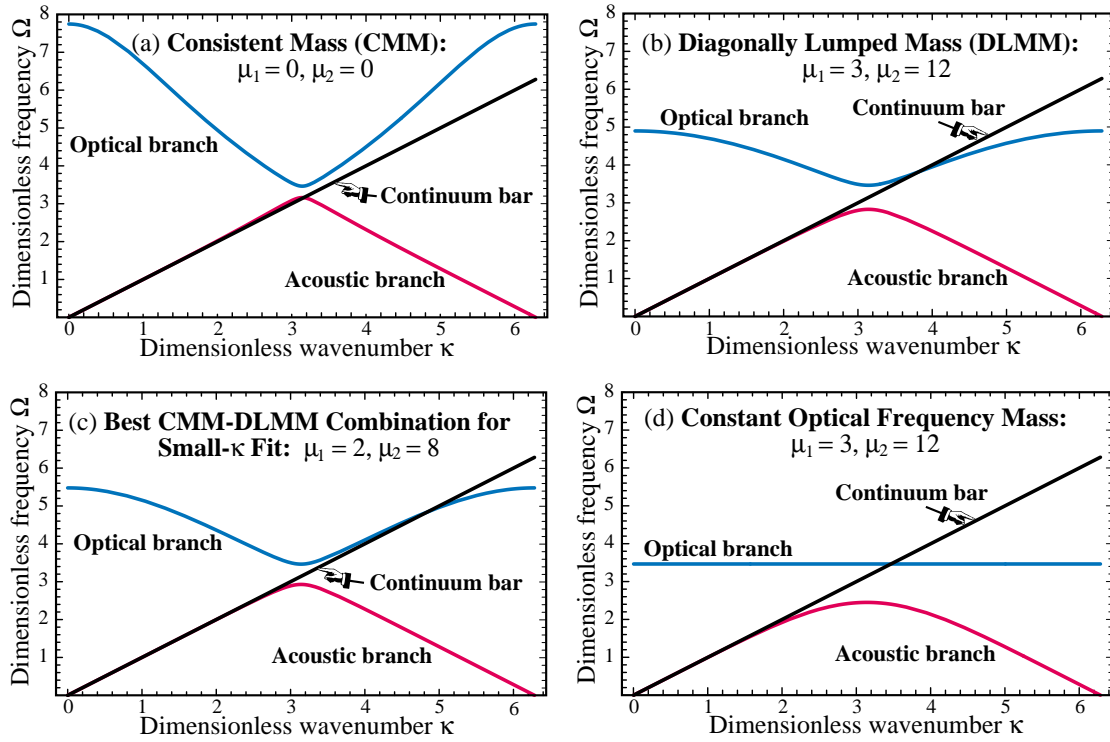
FIGURE 33.8. Dispersion curves of four mass matrices for the three-node prismatic bar, plotted for $\kappa \in [0, 2\pi]$. Acoustic branch in red, optical branch in blue, continuum bar line $\Omega = \kappa$ in black. Acoustic and optical branches repeat with period 2π; note symmetry about $\kappa = \pi$.

For a mass matrix to produce fourth order accuracy in the acoustic branch, $C_4 = 0$ in the series (33.31). This has the two solutions $\mu_2 = 4\mu_1$ and $\mu_2 = 4\mu_1 - 240$. Both CM and DLM comply with the first solution. To get sixth order accuracy for small κ we impose $C_4 = C_6 = 0$. This has only two solutions: $\{\mu_1 = 2, \mu_2 = 8\}$ and $\{\mu_1 = 62, \mu_2 = 8\}$. Only the first solution is of interest, as the second one produces large positive-negative entries and exactly the same dispersion curves. The resulting mass matrix turns out to be a linear combination of CMM and DLMM. It is labeled BLC for "best lumped-consistent combination":

$$
\mathbf{M}^e_{\text{BLC}} = \frac{\rho A \ell}{90} \begin{bmatrix} 14 & -1 & 2 \\ -1 & 14 & 2 \\ 2 & 2 & 56 \end{bmatrix} = \tfrac{1}{3}\mathbf{M}^e_C + \tfrac{2}{3}\mathbf{M}^e_L. \tag{33.33}
$$

As shown in Table 33.2, the acoustic branch of this matrix agrees up to $O(\kappa^6)$ with the continuum bar. The dispersion curves are shown in Figure 33.8(c).

A different kind of customization is advisable in dynamic simulations that involve propagation of high frequencies, such as shock and impact. The presence of the optical branch is undesirable, because it introduces spurious noise into the solutions. For such problems the two-node bar, which lacks an optical branch, should be used. If use of a three-node model is mandated for some reason, the harmful effects of the optical branch can be reduced by making it of constant frequency. Setting

$\{\mu_1 = 8, \mu_2 = 32\}$ produces the mass

$$\mathbf{M}^e_{\text{COF}} = \frac{\rho A \ell}{90} \begin{bmatrix} 10 & 5 & -10 \\ 5 & 10 & -10 \\ -10 & -10 & 80 \end{bmatrix}, \tag{33.34}$$

in which acronym COF stands for "Constant Optical Frequency." Then $\Omega_o^2 = 12$ for all wavenumbers, as pictured in Figure 33.8(d). This configuration maximizes the stopping band and facilitates the implementation of a narrow band filter centered at that frequency. The acoustic branch accuracy is inferior to that of the other models, however, so this customization involves a tradeoff.

One final parameter choice is worth mentioning as a curiosity. Setting $\{\mu_1 = -2, \mu_2 = -8\}$ produces a dispersion diagram *with no stopping band*: the optical branch comes down from $+\infty$ at $\kappa = 0, 2\pi$ and merges with the acoustic branch at $\kappa = \pi$. The application of this mass matrix (which is singular) as a modeling tool is presently unclear and its dispersion diagram is omitted.

§33.6. The Bernoulli-Euler Beam

The Bernoulli-Euler beam model is a special case of the Timoshenko beam treated in the next section. It is nonetheless useful to do its mass template first, since results provide a valuable cross check with the more complicated Timoshenko beam. We take the consistent mass matrix derived in the previous chapter, and modify their entries to produce the following entry-weighted template:

$$\mathbf{M}^e_\mu = \rho A \ell \begin{bmatrix} \frac{13}{35} + \mu_{11} & (\frac{11}{210} + \mu_{12})\ell & \frac{9}{70} + \mu_{13} & -(\frac{13}{420} + \mu_{14})\ell \\ & (\frac{1}{105} + \mu_{22})\ell^2 & (\frac{13}{420} + \mu_{23})\ell & -(\frac{1}{140} + \mu_{24})\ell^2 \\ & & \frac{13}{35} + \mu_{11} & -(\frac{11}{210} + \mu_{12})\ell \\ \text{symm} & & & (\frac{1}{105} + \mu_{22})\ell^2 \end{bmatrix} \tag{33.35}$$

The parameters in (33.35) are μ_{ij}, where ij identifies the mass matrix entry. The template (33.35) accounts for matrix symmetry and some physical symmetries. Three more conditions can be imposed right away: $\mu_{14} = \mu_{23}$, $\mu_{13} = -\mu_{11}$ and $2\mu_{12} = \mu_{11} + 2\mu_{22} + 2\mu_{23} - 2\mu_{24}$. The first comes from beam symmetry and the others from conservation of total translational mass and angular momentum, respectively. This reduces the free parameters to four: $\{\mu_{11}, \mu_{22}, \mu_{23}, \mu_{24}\}$. The Fourier analysis procedure should be familiar by now to the reader. An infinite lattice of identical beam elements of length ℓ is set up. Plane waves of wavenumber k and frequency ω propagating over the lattice are represented by

$$v(x, t) = B_v \exp\big(i(kx - \omega t)\big), \quad \theta(x, t) = B_\theta \exp\big(i(kx - \omega t)\big) \tag{33.36}$$

At a typical lattice node j there are two freedoms: v_j and θ_j. Two patch equations are extracted, and converted to dimensionless form on defining $\kappa = k\ell$ and $\Omega = \omega c_0/\ell$, in which $c_0 = EI/(\rho A \ell^4)$ is a reference phase velocity. The condition for wave propagation gives the characteristic matrix equation

$$\det \begin{bmatrix} C_{vv} & C_{v\theta} \\ C_{\theta v} & C_{\theta\theta} \end{bmatrix} = C_{vv} C_{\theta\theta} - C_{v\theta} C_{\theta v} = 0, \tag{33.37}$$

where $C_{vv} = \left(840 - 2(13 + 35\mu_{11})\Omega^2 - (840 + (9 - 70\mu_{11})\Omega^2)\cos\kappa\right)/35$, $-C_{\theta v} = C_{v\theta} = i\left(2520 + (13 + 420\mu_{23})\Omega^2\right)\sin\kappa/210$, $C_{\theta\theta} = \left(1680 - 4(1 + 105\mu_{22})\Omega^2 + (840 + 3(1 + 140\mu_{24})\Omega^2)\cos\kappa\right)/210$.
The condition (33.37) gives a quadratic equation in Ω^2 that provides two dispersion solutions: acoustical branch $\Omega_a^2(\kappa)$ and optical branch $\Omega_o^2(\kappa)$. These were already encountered in the analysis of the 3-node bar in §33.2. The acoustical branch represent genuine flexural modes, whereas the optical one is a spurious byproduct of the discretization. The small-κ (long wavelength) expansions of these roots are

$$\Omega_a^2 = \kappa^4 + C_6\kappa^6 + C_8\kappa^8 + C_{10}\kappa^{10} + C_{12}\kappa^{12} + \ldots, \quad \Omega_o^2 = D_0 + D_2\kappa^2 + D_4\kappa^4 + \ldots,$$
(33.38)

in which $C_6 = -\mu_{11} - 2\mu_{22} - 4\mu_{23} + 2\mu_{24}$, $C_8 = 1/720 + \mu_{11}^2 + 4\mu_{22}^2 + 2\mu_{23}/3 + 16\mu_{22}\mu_{23} + 16\mu_{23}^2 + \mu_{11}(1/12 + 4\mu_{22} + 8\mu_{23} - 4\mu_{24}) - \mu_{24} - 8\mu_{22}\mu_{24} - 16\mu_{23}\mu_{24} + 4\mu_{24}^2$, etc.; and $D_0 = 2520/(1 + 420\mu_{22} - 420\mu_{24})$, etc. *Mathematica* calculated these series up to C_{14} and D_4.

The continuum dispersion curve is $\Omega^2 = \kappa^4$, which automatically matches Ω_a^2 as $\kappa \to 0$. Thus four free parameters offer the opportunity to match coefficients of four powers: $\{\kappa^6, \kappa^8, \kappa^{10}, \kappa^{12}\}$. But it will be seen that the last match is unfeasible if $\mathbf{M}^e$ is to stay nonnegative. We settle for a scheme that agrees up to κ^{10}. Setting $C_6 = C_8 = C_{10} = 0$ while keeping μ_{22} free yields two sets of solutions, of which the useful one is

$$\mu_{11} = 4\mu_{22} - 67/540 - (4/27)\sqrt{38/35 - 108\mu_{22}},$$
$$\mu_{23} = 43/1080 - 2\mu_{22} + \sqrt{95/14 - 675\mu_{22}}/54,$$
$$\mu_{24} = 19/1080 - \mu_{22} + \sqrt{19/70 - 27\mu_{22}}/27.$$
(33.39)

The positivity behavior of $\mathbf{M}_\mu^e$ as μ_{22} is varied is shown in Figure 33.9(a). $\mathbf{M}^{(e)}$ is indefinite for $\mu_{22} < \mu_{22}^{min} = (27 - 4\sqrt{35})/5040 = 0.0006618414419844316$. At the other extreme the solutions of (33.39) become complex if $\mu_{22} > \mu_{22}^{max} = 19/1890 = 0.010052910052910053$.

Figure 33.9(b) plots $C_{12}(\mu_{22}) = (-111545 - 3008\psi + 15120(525 + 4\psi)\mu_{22})/685843200$, with $\psi = \sqrt{70}\sqrt{19 - 1890\mu_{22}}$. This has one real root $\mu_{22}^z = -0.02830257472322391$, but that gives an indefinite mass matrix. For μ_{22} in the legal range $[\mu_{22}^{min}, \mu_{22}^{max}]$, C_{12} is minimized for $\mu_{22}^b = (25\sqrt{105} - 171)/30240 = 0.0028165928951385567$, which substituted gives the optimal mass matrix:

$$\mathbf{M}_B^e = \frac{\rho A\ell}{30240}\begin{bmatrix} a_{11} & 1788\ell & a_{13} & -732\ell \\ & a_{22}\ell^2 & 732\ell & a_{24}\ell^2 \\ & & a_{33} & 1788\ell \\ \text{symm} & & & a_{44}\ell^2 \end{bmatrix} = \rho A\ell\begin{bmatrix} 0.389589 & 0.059127\ell & 0.110410 & -0.024206\ell \\ & 0.012340\ell^2 & 0.024206\ell & -0.005548\ell^2 \\ & & 0.389589 & -0.059127\ell \\ & & & 0.012340\ell^2 \end{bmatrix}$$
(33.40)

in which $a_{11} = a_{33} = 12396 - 60\sqrt{105}$, $a_{13} = 2724 + 60\sqrt{105}$, $a_{22} = a_{44} = 117 + 25\sqrt{105}$ and $a_{24} = -219 + 5\sqrt{105}$. For this set, $C_{12} = (25\sqrt{105} - 441)/91445760 = -2.02\,10^{-6}$. Another interesting value is $\mu_{22} = 13/3150 = 0.004126984126984127$, which substituted in (33.39) yields rational values for the other parameters: $\mu_{11} = -\mu_{13} = 23/2100$, $\mu_{12} = -\mu_{14} = -\mu_{23} = 23/4200$, $\mu_{24} = 23/4200$ and $\mu_{24} = -17/12600$. Replacing into the template gives
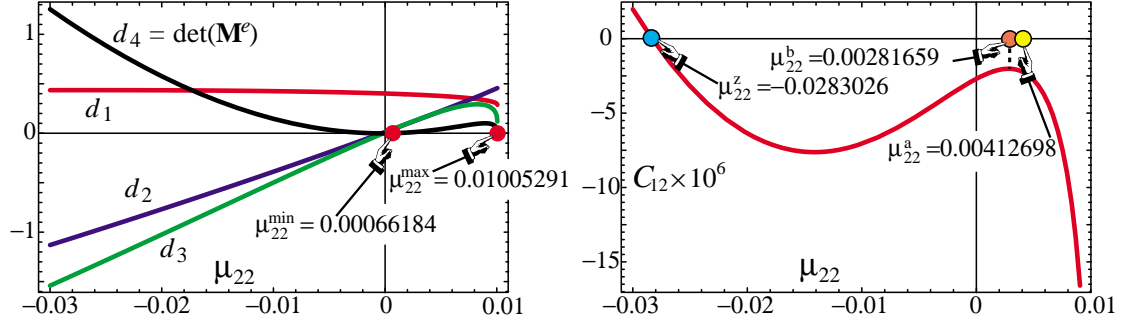
FIGURE 33.9. Behavior of $\mathbf{M}_\mu^e$ as function of μ_{22} when other μ parameters are picked from (33.39): (a) determinants d_k of principal minors of order k of $\mathbf{M}_\mu^e$, showing legal positivity range $\{\mu_{22}^{min}, \mu_{22}^{max}\}$; (b) coefficient C_{12} of κ^{12} in Ω_a^2 series.

$$\mathbf{M}_Q^e = \frac{\rho A \ell}{12600} \begin{bmatrix} 4818 & 729\ell & 1482 & -321\ell \\ & 172\ell^2 & 321\ell & -73\ell^2 \\ & & 4818 & -729\ell \\ \text{symm} & & & 172\ell^2 \end{bmatrix} = \rho A \ell \begin{bmatrix} 0.382381 & 0.057857\ell & 0.117619 & -0.025476\ell \\ & 0.013651\ell^2 & 0.025476\ell & -0.005794\ell^2 \\ & & 0.382381 & -0.057857\ell \\ \text{symm} & & & 0.013651\ell^2 \end{bmatrix}$$
(33.41)

For this matrix, $C_{12} = -41/18144000 = -2.25 \, 10^{-6}$, which is only about 10% higher than for the optimal mass. Since the entries are simpler, (33.41) is adopted as custom mass matrix and used as a baseline for the Timoshenko beam.

§33.7. *Two-Node Timoshenko Beam Element

The last example is far more elaborate than the previous ones. The goal is to construct a mass template for the prismatic, plane-beam Timoshenko model. This includes the Bernoulli-Euler model as special case, and consequently results can be crosschecked with those of the previous section. The continuum Timoshenko model is first examined in some detail, since frequency expansion formulas applicable to template customization by characteristic root fitting are not easily found in the literature.

§33.7.1. *Continuum Analysis

Consider a structural beam member modeled as a shear-flexible Timoshenko plane beam, as illustrated in Figure 33.10. This figure provides the notation used below. Section properties $\{\rho, E, A, A_s, I, I_R\}$ are constant along x. The beam is transversely loaded by line load $q(x, t)$ (not shown in figure), with dimension of force per length. The primary kinematic variables are the transverse deflection $v(x, t)$ and the total cross-section rotation $\theta(x, t) = v'(x, t) + \gamma(x, t)$, where $\gamma = V/(GA_s)$ is the mean shear rotation. The kinetic and potential energies in terms of those variables are

$$T[v, \theta] = \tfrac{1}{2} \int_0^L \left(\rho A \, \dot{v}^2 + \rho I_R \, \dot{\theta}^2 \right) dx, \quad \Pi[v, \theta] = \int_0^L \left(\tfrac{1}{2} EI (v'')^2 + \tfrac{1}{2} GA_s (\theta - v')^2 - qv \right) dx. \quad (33.42)$$

where superposed dots denote time derivatives. The equations of motion (EOM) follow on forming the Euler-Lagrange equations from the Lagrangian $L = T - \Pi$:

$$\frac{\delta L}{\delta v} = 0 \to GA_s (\theta' - v'') + \rho A \ddot{v} = q, \quad \frac{\delta L}{\delta \theta} = 0 \to EI \, \theta'' + GA_s (v' - \theta) - \rho I_R \ddot{\theta} = 0. \quad (33.43)$$
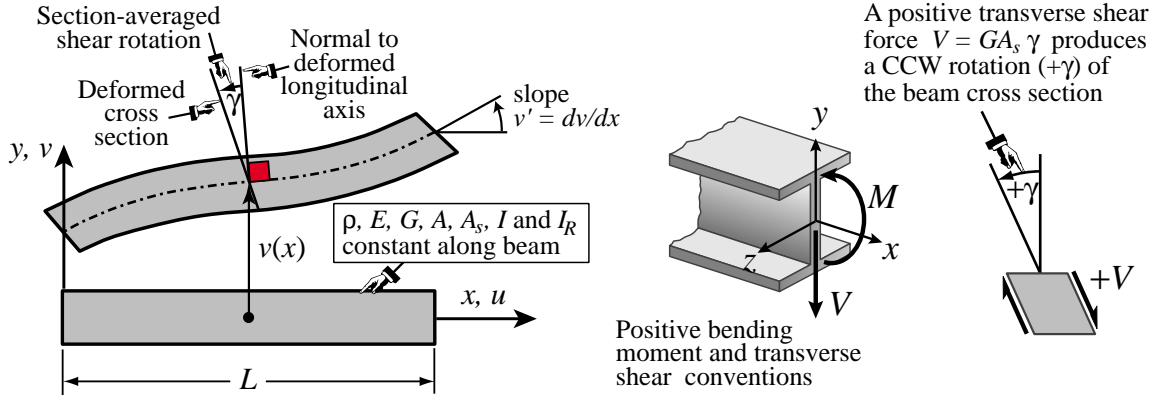
FIGURE 33.10. A plane beam member modeled as Timoshenko beam, illustrating notation followed in the continuum analysis. Transverse load $q(x)$ not shown to reduce clutter. Infinitesimal deflections and deformations grossly exaggerated for visibility.

An expedient way to eliminate θ is to rewrite the coupled equations (33.43) in transform space:

$$\begin{bmatrix} \rho A s^2 - GA_s\, p^2 & GA_s\, p \\ GA_s\, p & EI\, p^2 - GA_s - \rho\, I_R\, s^2 \end{bmatrix} \begin{bmatrix} \tilde{v} \\ \tilde{\theta} \end{bmatrix} = \begin{bmatrix} \tilde{q} \\ 0 \end{bmatrix}, \tag{33.44}$$

in which $\{p, s, \tilde{v}, \tilde{\theta}, \tilde{q}\}$ denote transforms of $\{d/dx, d/dt, v, \theta, q\}$, respectively (Fourier in x and Laplace in t). Eliminating $\tilde{\theta}$ and returning to the physical domain yields

$$EI\, v'''' + \rho A \ddot{v} - \left(\rho I_R + \frac{\rho A E I}{GA_s} \right) \ddot{v}'' + \frac{\rho^2 A I_R}{GA_s} \ddddot{v} = q - \frac{EI}{GA_s} q'' + \frac{\rho I_R}{GA_s} \ddot{q}. \tag{33.45}$$

(Note that this derivation does not pre-assume $I \equiv I_R$, as usually done in textbooks.) For the unforced case $q = 0$, (33.45) has plane wave solutions $v = B \exp\big(i\,(k_0\, x - \omega_0\, t) \big)$. The propagation condition yields a characteristic equation relating k_0 and ω_0. To render it dimensionless, introduce a reference phase velocity $c_0^2 = EI/(\rho A L^4)$ so that $k_0 = \omega_0/c_0 = 2\pi/\lambda_0$, a dimensionless frequency $\Omega = \omega_0 L/c_0$ and a dimensionless wavenumber $\kappa = k_0 L$. As dimensionless measures of relative bending-to-shear rigidities and rotary inertia take

$$\Phi_0 = 12EI/(GA_s L^2), \qquad r_R^2 = I_R/A, \qquad \Psi_0 = r_R/L. \tag{33.46}$$

The resulting dimensionless characteristic equation is

$$\kappa^4 - \Omega^2 - (\tfrac{1}{12}\Phi_0 + \Psi_0^2)\,\kappa^2\,\Omega^2 + \tfrac{1}{12}\Phi_0\,\Psi_0^2\,\Omega^4 = 0. \tag{33.47}$$

This is quadratic in Ω^2. Its solution yields two kinds of squared-frequencies, which will be denoted by Ω_f^2 and Ω_s^2 because they are associated with flexural and shear modes, respectively. Their expressions are listed below along with their small-κ (long wavelength) Taylor series:

$$\Omega_f^2 = 6\frac{P - \sqrt{Q}}{\Phi_0 \Psi_0^2} = \kappa^4 - (\tfrac{1}{12}\Phi_0 + \Psi_0^2)\,\kappa^6 + (\tfrac{1}{144}\Phi_0^2 + \tfrac{1}{4}\Phi_0\Psi_0^2 + \Psi_0^4)\,\kappa^8$$
$$- (\tfrac{1}{1728}\Phi_0^3 + \tfrac{1}{24}\Phi_0^2\Psi_0^2 + \tfrac{1}{2}\Phi_0\Psi_0^4 + \Psi_0^6)\,\kappa^{10} + \ldots = A_4\kappa^4 + A_6\kappa^6 + A_8\kappa^8 + \ldots \tag{33.48}$$

$$\Omega_s^2 = 6\frac{P + \sqrt{Q}}{\Phi_0 \Psi_0^2} = \frac{12}{\Phi_0 \Psi_0^2} + \left(\frac{12}{\Phi_0} + \frac{1}{\Psi_0^2} \right)\kappa^2 - \kappa^4 + (\tfrac{1}{12}\Phi_0 + \Psi_0^2)\kappa^6 + \ldots = B_0 + B_2\kappa^2 + \ldots \tag{33.49}$$

in which $P = 1 + \kappa^2(\Psi_0^2 + \tfrac{1}{12}\Phi_0)$ and $Q = P^2 - \tfrac{1}{3}\kappa^4\Phi_0\Psi_0^2$. The dispersion relation $\Omega_f^2(\kappa)$ defines the *flexural frequency branch* whereas $\Omega_s^2(\kappa)$ defines the *shear frequency branch*. If $\Phi_0 \to 0$ and $\Psi_0 \to 0$, which
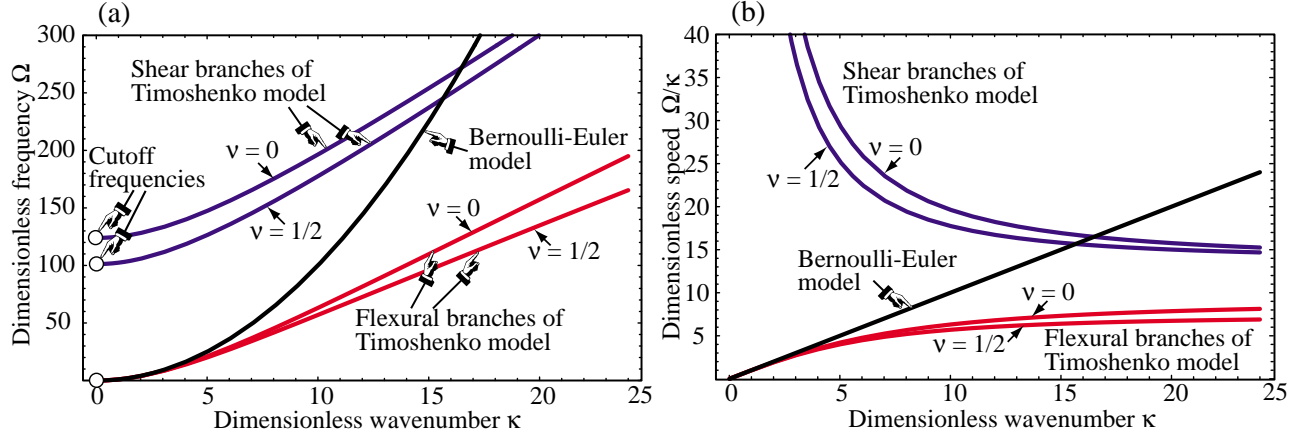
FIGURE 33.11. Spectral behavior of continuum Timoshenko beam model for a narrow $b \times h$ rectangular cross section. (a): dispersion curves $\Omega(\kappa)$ for $\Lambda = h/\ell = 1/4$ and two Poisson's ratios; Timoshenko flexural and shear branches in red and blue, respectively; Bernoulli-Euler curve $\Omega = \kappa^2$ in black. (b) Wavespeed Ω/κ.

reduces the Timoshenko model to the Bernoulli-Euler one, (33.47) collapses to $\Omega^2 = \kappa^4$ or (in principal value) $\Omega = \kappa^2$. This surviving branch pertains to flexural motions while the shear branch disappears — or more precisely, $\Omega_s^2(\kappa) \to +\infty$. It is easily shown that the radicand Q in the exact expressions is strictly positive for any $\{\Phi_0 > 0, \Psi_0 > 0, \kappa \geq 0\}$. Thus for any such triple, Ω_f^2 and Ω_s^2 are real, finite and distinct with $\Omega_f^2(\kappa) < \Omega_s^2(\kappa)$; furthermore $\{\Omega_f^2, \Omega_s^2\}$ increase indefinitely as $\kappa \to \infty$. Following the nomenclature introduced in Figure 33.7, the value Ω_s at $\kappa = 0$ is called the cutoff frequency.

To see how branches look like, consider a beam of narrow rectangular cross section of width b and height h, fabricated of isotropic material with Poisson's ratio ν. We have $E/G = 2(1 + \nu)$ and $A_s/A \approx 5/6$. [Actually a more refined A_s/A ratio would be $10(1 + \nu)/(12 + 11\nu)$, but that makes little difference in the results.] We have $A = bh$, $I = I_R = bh^3/12$, $r_R^2 = I_R/A = h^2/12$, $\Psi_0^2 = r_R^2/L^2 = \frac{1}{12}h^2/L^2$ and $\Phi_0 = 12EI/(GA_sL^2) = 12(1 + \nu)h^2/(5L^2)$. Since $\Phi_0/12 = 12(1 + \nu)\Psi_0^2/5$, the first-order effect of shear on Ω_f^2, as measured by the κ^6 term in (33.48), is 2.4 to 3.6 times that from rotary inertia, depending on ν. Replacing into (33.48) and (33.49) yields

$$
\left.\begin{array}{l} \Omega_f^2 \\ \Omega_s^2 \end{array}\right\} = \frac{60 + \kappa^2(17 + 12\nu)\Lambda^2 \mp \sqrt{\left(60 + \kappa^2(17 + 12\nu)\Lambda^2\right)^2 - 240\kappa^4(1 + \nu)\Lambda^4}}{2(1 + \nu)\Lambda^4}
$$

$$
= \begin{cases} \kappa^4 - \frac{1}{60}(17 + 12\nu)\Lambda^2\kappa^6 + \frac{1}{3600}(349 + 468\nu + 144\nu^2)\Lambda^4\kappa^8 + \ldots \\ \dfrac{60 + (17 + 12\nu)\Lambda^2\kappa^2 - (1 + \nu)\Lambda^4\kappa^4 + \ldots}{(1 + \nu)\Lambda^4} \end{cases} \tag{33.50}
$$

in which $\Lambda = h/L$. Dispersion curves $\Omega(\kappa)$ for $\Lambda = h/L = 1/4$ and $\nu = \{0, 1/2\}$ are plotted in Figure 33.11(a). Phase velocities Ω/κ are shown in Figure 33.11(b). The figure also shows the flexural branch of the Bernoulli-Euler model. The phase velocities of the Timoshenko model tend to finite values in the shortwave, high-frequency limit $\kappa \to \infty$, which is physically correct. The Bernoulli-Euler model is wrong in that limit because it predicts an infinite propagation speed.

§33.7.2. *Beam Element

The shear-flexible plane beam member of Figure 33.10 is discretized by two-node elements. An individual element of this type is shown in Figure 33.12, which illustrates its kinematics. The element has four nodal freedoms arranged as

$$\mathbf{u}^e = [\, v_1 \;\; \theta_1 \;\; v_2 \;\; \theta_2 \,]^T \qquad (33.51)$$

Here $\theta_1 = v_1' + \gamma_1$ and $\theta_2 = v_2' + \gamma_2$ are the total cross section rotations evaluated at the end nodes.

FIGURE 33.12. Two-node element for Timoshenko plane beam, illustrating kinematics.

The dimensionless properties (33.46) that characterize relative shear rigidity and rotary inertia are redefined using the element length:

$$\Phi = 12EI/(GA_s\ell^2), \qquad r_R^2 = I_R/A, \qquad \Psi = r_R/\ell. \qquad (33.52)$$

If the beam member is divided into N_e elements of equal length, $\ell = L/N_e$ whence $\Phi = \Phi_0 N_e^2$ and $\Psi = \Psi_0 N_e$. Thus even if Φ_0 and Ψ_0 are small with respect to one, they can grow without bound as the mesh is refined. For example if $\Phi_0 = 1/4$ and $\Psi_0^2 = 1/100$, which are typical values for a moderately thick beam, and we take $N_e = 32$, then $\Phi \approx 250$ and $\Psi^2 \approx 10$. Those are no longer small numbers, a fact that will impact performance as N_e increases. The stiffness matrix to be paired with the mass template is taken to be that of the equilibrium element:

$$\mathbf{K}^e = \frac{EI}{\ell^3(1+\Phi)} \begin{bmatrix} 12 & 6\ell & -12 & 6\ell \\ 6\ell & \ell^2(4+\Phi) & -6\ell & \ell^2(2-\Phi) \\ -12 & -6\ell & 12 & -6\ell \\ 6\ell & \ell^2(2-\Phi) & -6\ell & \ell^2(4+\Phi) \end{bmatrix} \qquad (33.53)$$

This is known to be nodally exact in static analysis for a prismatic beam member, and therefore an optimal choice in that sense.

§33.7.3. *Setting Up the Mass Template

FEM derivations usually split the 4×4 mass matrix of this element into $\mathbf{M}^e = \mathbf{M}_v^e + \mathbf{M}_\theta^e$, where $\mathbf{M}_v^e$ and $\mathbf{M}_\theta^e$ come from the translational inertia and rotary inertia terms, respectively, of the kinetic energy functional $T[v,\theta]$ of (33.42). The most general mass template would result from applying a entry-weighted parametrization of those two matrices. This would require a set of 20 parameters (10 in each matrix), reducible to 9 through 11 on account of invariance and conservation conditions. Attacking the problem this way, however, leads to unwieldy algebraic equations even with the help of a computer algebra system, while concealing the underlying physics. A divide and conquer approach works better. This is briefly outlined next and covered in more detail in the next subsections.

(I) Express $\mathbf{M}^e$ as the one-parameter matrix-weighted form $\mathbf{M}^e = (1-\mu_0)\,\mathbf{M}_F^e + \mu_0\,\mathbf{M}_D^e$. Here $\mathbf{M}_F^e$ is full and includes the CMM as instance, whereas $\mathbf{M}_D^e$ is 2×2 block diagonal and includes the DLMM as instance. This is plainly a generalization of the LC linear combination (33.2).

(II) Decompose the foregoing mass components as $\mathbf{M}_F^e = \mathbf{M}_{FT}^e + \mathbf{M}_{FR}$ and $\mathbf{M}_D^e = \mathbf{M}_{DT}^e + \mathbf{M}_{DR}^e$, where T and R subscripts identify their source in the kinetic energy functional: T if coming from the translational inertia term $\frac{1}{2}\rho A\,\dot{v}^2$ and R from the rotary inertia term $\frac{1}{2}\rho I_R\,\dot{\theta}^2$.

(III) Both components of $\mathbf{M}_F^e$ are expressed as parametrized spectral forms, whereas those of $\mathbf{M}_D^e$ are expressed as entry-weighted. The main reasons for choosing spectral forms for the full matrix are reduction of parameters and physical transparency. No such concerns apply to $\mathbf{M}_D^e$.

The analysis follows a "bottom up" sequence, in order (III)-(II)-(I). This has the advantage that if a satisfactory custom mass matrix for a target application emerges during (III), stages (II) and (I) need not be carried out, and that matrix directly used by setting the remaining parameters to zero.
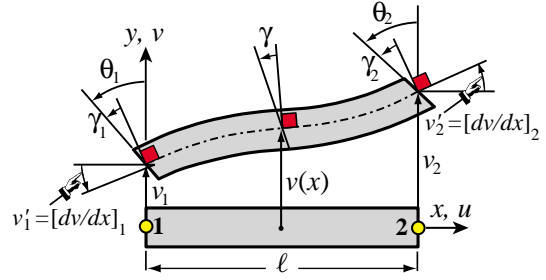
§33.7.4. *Full Mass Parametrization

As noted above, one starts with full-matrix spectral forms. Let ξ denote the natural coordinate that varies from -1 at node 1 to $+1$ at node 2. Two element transverse displacement expansions in generalized coordinates are introduced:

$$
\begin{aligned}
v_T(\xi) &= L_1(\xi)\, c_{T1} + L_2(\xi)\, c_{T2} + L_3(\xi)\, c_{T3} + L_4(\xi)\, c_{T4} = \mathbf{L}_T\, \mathbf{c}_T, \\
v_R(\xi) &= L_1(\xi)\, c_{R1} + L_2(\xi)\, c_{R2} + L_3(\xi)\, c_{R3} + \widehat{L}_4(\xi)\, c_{R4} = \mathbf{L}_R\, \mathbf{c}_R, \\
L_1(\xi) &= 1, \ \ L_2(\xi) = \xi, \ \ L_3(\xi) = \tfrac{1}{2}(3\xi^2 - 1), \ \ L_4(\xi) = \tfrac{1}{2}(5\xi^3 - 3\xi), \\
\widehat{L}_4(\xi) &= \tfrac{1}{2}\big(5\xi^3 - (5 + 10\Phi)\xi\big) = L_4(\xi) - (1 + 5\Phi)\xi.
\end{aligned}
\tag{33.54}
$$

The v_T and v_R expansions are used for the translational and rotational parts of the kinetic energy, respectively. The interpolation function set $\{L_i\}$ used for v_T is formed by the first four Legendre polynomials over $\xi = [-1, 1]$. The set used for v_R is the same except that L_4 is adjusted to $\widehat{L}_4$ to produce a diagonal rotational mass matrix. All amplitudes c_{Ti} and c_{Ri} have dimension of length.

Unlike the usual Hermite cubic shape functions, the polynomials in (33.54) have a direct physical interpretation. L_1: translational rigid mode; L_2: rotational rigid mode; L_3: pure-bending mode symmetric about $\xi = 0$; L_4 and $\widehat{L}_4$: bending-with-shear modes antisymmetric about $\xi = 0$.

With the usual abbreviation $(.)' \equiv d(.)/dx = (2/\ell)d(.)/d\xi$, the associated cross section rotations are

$$
\theta_T = v_T' + \gamma_T = \mathbf{L}_T'\mathbf{c}_T + \gamma_T, \quad \theta_R = v_R' + \gamma_R = \mathbf{L}_R'\,\mathbf{c}_R + \gamma_R,
\tag{33.55}
$$

in which the mean shear distortions are constant over the element:

$$
\gamma_T = \frac{\Phi\ell^2}{12}v_T''' = \frac{10\Phi}{\ell}c_{T4}, \quad \gamma_R = \frac{\Phi\ell^2}{12}v_R''' = \frac{10\Phi}{\ell}c_{R4}.
\tag{33.56}
$$

The kinetic energy of the element in generalized coordinates is

$$
T^e = \tfrac{1}{2}\int_0^\ell \left(\rho A\,\dot{v}_T^2 + \rho I_R\,\dot{\theta}_R^2\right)dx = \frac{\ell}{4}\int_{-1}^1 \left(\rho A\,\dot{v}_T^2 + \rho I_R\,\dot{\theta}_R^2\right)d\xi = \tfrac{1}{2}\dot{\mathbf{c}}_T^T\,\mathbf{D}_T\,\dot{\mathbf{c}}_T + \tfrac{1}{2}\dot{\mathbf{c}}_R^T\,\mathbf{D}_R\,\dot{\mathbf{c}}_R,
\tag{33.57}
$$

in which both generalized mass matrices turn out to be diagonal as intended:

$$
\mathbf{D}_T = \rho A\ell\,\mathbf{diag}\,[\,1 \ \ \tfrac{1}{3} \ \ \tfrac{1}{5} \ \ \tfrac{1}{7}\,], \quad \mathbf{D}_R = 4\rho A\ell\Psi^2\,\mathbf{diag}\,[\,0 \ \ 1 \ \ 3 \ \ 5\,].
$$

To convert $\mathbf{D}_T$ and $\mathbf{D}_R$ to physical coordinates (33.51), v_T, v_R, θ_T and θ_R are evaluated at the nodes by setting $\xi = \pm 1$. This establishes the transformations $\mathbf{u}^e = \mathbf{G}_T\,\mathbf{c}_T$ and $\mathbf{u}^e = \mathbf{G}_R\,\mathbf{c}_R$. Inverting: $\mathbf{c}_T = \mathbf{H}_T\,\mathbf{u}^e$ and $\mathbf{c}_R = \mathbf{H}_R\,\mathbf{u}^e$ with $\mathbf{H}_T = \mathbf{G}_T^{-1}$ and $\mathbf{H}_R = \mathbf{G}_R^{-1}$. A symbolic calculation yields

$$
\begin{aligned}
\mathbf{H}_T &= \frac{1}{60(1+\Phi)}
\begin{bmatrix}
30(1+\Phi) & 5\ell(1+\Phi) & 30(1+\Phi) & -5\ell(1+\Phi) \\
-36 - 30\Phi & -3\ell & 36 + 30\Phi & -3\ell \\
0 & -5\ell(1+\Phi) & 0 & 5\ell(1+\Phi) \\
6 & 3\ell & -6 & 3\ell
\end{bmatrix} \\[1em]
\mathbf{H}_R &= \frac{1}{60(1+\Phi)}
\begin{bmatrix}
30(1+\Phi) & 5\ell(1+\Phi) & 30(1+\Phi) & -5\ell(1+\Phi) \\
-30 & 15\ell\Phi & 30 & 15\ell\Phi \\
0 & -5\ell(1+\Phi) & 0 & 5\ell(1+\Phi) \\
6 & 3\ell & -6 & 3\ell
\end{bmatrix}
\end{aligned}
\tag{33.58}
$$

Matrices $\mathbf{H}_T$ and $\mathbf{H}_R$ differ only in the second row. This comes from the adjustment of L_4 to $\widehat{L}_4$ in (33.54). To render this into a spectral template inject six free parameters in the generalized masses while moving $4\Psi^2$ inside $\mathbf{D}_{R\mu}$:

$$
\mathbf{D}_{T\mu} = \rho A\ell\,\mathbf{diag}\,[\,1 \ \ \tfrac{1}{3}\mu_{T1} \ \ \tfrac{1}{5}\mu_{T2} \ \ \tfrac{1}{7}\mu_{T3}\,], \quad \mathbf{D}_{R\mu} = \rho A\ell\,\mathbf{diag}\,[\,0 \ \ \mu_{R1} \ \ 3\mu_{R2} \ \ 5\mu_{R3}\,].
\tag{33.59}
$$

The transformation matrices (33.58) are reused without change to produce $\mathbf{M}_F^e = \mathbf{H}_T^T \mathbf{D}_{T\mu} \mathbf{H}_T + \mathbf{H}_R^T \mathbf{D}_{R\mu} \mathbf{H}_R$. If $\mu_{T1} = \mu_{T2} = \mu_{T3} = 1$ and $\mu_{R1} = \mu_{R2} = \mu_{R3} = 4\Psi^2$ one obtains the well known consistent mass matrix (CMM) of Archer, listed in [205, p. 296], as a valuable check. The configuration (33.59) already accounts for linear momentum conservation, which is why the upper diagonal entries are not parametrized. Imposing also angular momentum conservation requires $\mu_{T1} = 1$ and $\mu_{R1} = 4\Psi^2$, whence the template is reduced to four parameters:

$$
\mathbf{M}_F^e = \rho A \ell \, \mathbf{H}_T^T
\begin{bmatrix}
1 & 0 & 0 & 0 \\
0 & \frac{1}{3} & 0 & 0 \\
0 & 0 & \frac{1}{5}\mu_{T2} & 0 \\
0 & 0 & 0 & \frac{1}{7}\mu_{T3}
\end{bmatrix}
\mathbf{H}_T + \rho A \ell \, \mathbf{H}_R^T
\begin{bmatrix}
0 & 0 & 0 & 0 \\
0 & 4\Psi^2 & 0 & 0 \\
0 & 0 & 3\mu_{R2} & 0 \\
0 & 0 & 0 & 5\mu_{R3}
\end{bmatrix}
\mathbf{H}_R. \tag{33.60}
$$

Because both $\mathbf{H}_T$ and $\mathbf{H}_R$ are nonsingular, choosing all four parameters in (33.60) to be nonnegative guarantees that $\mathbf{M}_F^e$ is nonnegative. This useful property eliminates lengthy *a posteriori* checks.

Setting $\mu_{T2} = \mu_{T3} = \mu_{R2} = \mu_{R3} = 0$ and $\Phi = 0$ yields the correct mass matrix for a rigid beam, including rotary inertia. This simple result highlights the physical transparency of spectral forms.

§33.7.5. *Block-Diagonal Mass Parametrization

Template (33.60) has a flaw: it does not include the DLMM. To remedy the omission, a block diagonal form, with four free parameters: $\{\nu_{T1}, \nu_{T2}, \nu_{R1}, \nu_{R2}\}$. is separately constructed:

$$
\mathbf{M}_D^e = \mathbf{M}_{DT} + \mathbf{M}_{DR} = \rho A \ell
\begin{bmatrix}
\frac{1}{2} & \nu_{T1}\ell & 0 & 0 \\
\nu_{T1}\ell & \nu_{T2}\ell^2 & 0 & 0 \\
0 & 0 & \frac{1}{2} & -\nu_{T1}\ell \\
0 & 0 & -\nu_{T1}\ell & \nu_{T2}\ell^2
\end{bmatrix}
+ \rho A \ell
\begin{bmatrix}
0 & \nu_{R1}\ell & 0 & 0 \\
\nu_{R1}\ell & \nu_{R2}\ell^2 & 0 & 0 \\
0 & 0 & 0 & -\nu_{R1}\ell \\
0 & 0 & -\nu_{R1}\ell & \nu_{R2}\ell^2
\end{bmatrix} \tag{33.61}
$$

Four parameters can be merged into two by adding:

$$
\mathbf{M}_D^e = \rho A \ell
\begin{bmatrix}
\frac{1}{2} & \nu_1\ell & 0 & 0 \\
\nu_1\ell & \nu_2\ell^2 & 0 & 0 \\
0 & 0 & \frac{1}{2} & -\nu_1\ell \\
0 & 0 & -\nu_1\ell & \nu_2\ell^2
\end{bmatrix}. \tag{33.62}
$$

where $\nu_1 = \nu_{T1} + \nu_{R1}$ and $\nu_2 = \nu_{T2} + \nu_{R2}$. Sometimes it is convenient to use the split form (33.61), for example in lattices with varying beam properties or lengths, a topic not considered there. Otherwise (33.62) suffices. If $\nu_1 = 0$, $\mathbf{M}_D^e$ is diagonal. However for computational purposes a block diagonal form is just as good and provides additional customization power. Terms in the (1,1) and (3,3) positions must be as shown to satisfy linear momentum conservation. If angular momentum conservation is imposed *a priori* it is necessary to set $\nu_2 = \frac{1}{2}\Psi^2$, and only one parameter remains.

The general template is obtained as a linear combination of $\mathbf{M}_F^e$ and $\mathbf{M}_D^e$:

$$
\mathbf{M}^e = (1 - \mu_0)\mathbf{M}_F^e + \mu_0 \mathbf{M}_D^e \tag{33.63}
$$

Summarizing there is a total of 7 parameters to play with: 4 in $\mathbf{M}_F^e$, 2 in $\mathbf{M}_D^e$, plus μ_0. This is less that the 9-to-11 that would result from a full entry-weighted parametrization, so not all possible mass matrices are included by (33.63).

§33.7.6. *Fourier Analysis

An infinite lattice of identical beam elements of length ℓ is set up. Plane waves of wavenumber k and frequency ω propagating over the lattice are represented by

$$v(x, t) = B_v \exp\left(i(kx - \omega t)\right), \quad \theta(x, t) = B_\theta \exp\left(i(kx - \omega t)\right) \tag{33.64}$$

At each typical lattice node j there are two freedoms: v_j and θ_j. Two patch equations are extracted, and converted to dimensionless form on defining $\kappa = k\ell$ and $\Omega = \omega c/\ell$, in which $c = EI/(\rho A \ell^4)$ is a reference phase velocity. (Do not confuse with c_0). The condition for wave propagation gives the characteristic matrix equation

$$\det \begin{bmatrix} C_{vv} & C_{v\theta} \\ C_{\theta v} & C_{\theta\theta} \end{bmatrix} = C_{vv} C_{\theta\theta} - C_{v\theta} C_{\theta v} = 0, \tag{33.65}$$

where the coefficients are complicated functions not listed there. Solving the equation provides two equations: Ω_a^2 and Ω_o^2, where a and o denote acoustic and optical branch, respectively. These are expanded in powers of κ for matching to the continuum. For the full mass matrix one obtains

$$\Omega_a^2 = \kappa^4 + C_6 \kappa^6 + C_8 \kappa^8 + C_{10} \kappa^{10} + \ldots, \quad \Omega_o^2 = D_0 + D_2 \kappa^2 + \ldots \tag{33.66}$$

Coefficients up to κ^{12} were computed by *Mathematica*. Relevant ones for parameter selection are

$$
\begin{aligned}
C_6 &= -\Phi/12 - \Psi^2, \\
C_8 &= \left[2 - 15\mu_{R2} - \mu_{T2} + 5\Phi(1 + \Phi) + 60(1 + 3\Phi)\Psi^2 + 720\Psi^4\right]/720, \\
C_{10} &= \Big[-44 + 35\mu_{T2} - 3\mu_{T3} - 282\Phi + 525\mu_{R2}(1 + \Phi) - 105\mu_{R3}(1 + \Phi) + \\
&\quad 1575\mu_{R2}\Phi(1 + \Phi) - \Phi(3\mu_{T3} - 35\mu_{T2}(4 + 3\Phi) + 35\Phi(17 + 5\Phi(3 + \Phi))) + \\
&\quad (-2940 + 12600\mu_{R2}(1 + \Phi) + 420(2\mu_{T2}(1 + \Phi) - 5\Phi(7 + 6\Phi(2 + \Phi))))\Psi^2 - \\
&\quad 25200(2 + \Phi(7 + 6\Phi))\Psi^4 - 302400(1 + \Phi)\Psi^6\Big]/\left[302400(1 + \Phi)\right], \\
D_0 &= 25200(1 + \Phi)/\left[7 + 105\mu_{R2} + 3\mu_{T3} + 2100\Phi^2\Psi^2\right], \\
D_2 &= \Big[2100(1 + \Phi)(-56 - 35\mu_{T2} + 3\mu_{T3} - 63\Phi + 3\mu_{T3}\Phi + 105\mu_{R3}(1 + \Phi) - \\
&\quad 525\mu_{R2}(1 + \Phi)^2 - 35\mu_{T2}\Phi(2 + \Phi)) + 2100(1 + \Phi)(3360\Phi + 6300\Phi^2 + \\
&\quad 2100\Phi^3)\Psi^2 + 52920000\Phi^2(1 + \Phi)\Psi^4\Big]/\left[7 + 105\mu_{R2} + 3\mu_{T3} + 2100\Phi^2\Psi^2\right]^2
\end{aligned}
\tag{33.67}
$$

For the block-diagonal template (33.62):

$$\Omega_a^2 = \kappa^4 + F_6 \kappa^6 + F_8 \kappa^8 + F_{10} \kappa^{10} + \ldots, \quad \Omega_o^2 = G_0 + G_2 \kappa^2 + \ldots \tag{33.68}$$

where

$$
\begin{aligned}
F_6 &= -24v_2 - \Phi, \quad F_8 = \frac{2880v_2 - 5\Phi + 360v_2\Phi - 1 - 5\Phi + 5\Phi^2}{720} \\
G_0 &= \frac{6}{v_2(1 + \Phi)}, \quad G_2 = \frac{24v_2 + \Phi - 2}{2v_2(1 + \Phi)}
\end{aligned}
\tag{33.69}
$$

The expansions for the 7-parameter template (33.63) are considerably more complicated than the above ones, and are omitted to save space.

Table 33.3. Useful Template Instances for Timoshenko Beam Element

Instance name	Description	Comments
CMM	Consistent mass matrix of Archer. Matches flexural branch up to $O(\kappa^6)$.	A popular choice. Fairly inaccurate, however, as beam gets thicker. Grossly overestimates intermediate frequencies.
FBMS	Flexural-branch matched to $O(\kappa^{10})$ with spectral (Legendre) template (33.60).	Converges faster than CMM. Performance degrades as beam gets thicker, however, and element becomes inferior to CDLA.
SBM0	Shear branch matched to $O(\kappa^0)$ while flexure fitted to $O(\kappa^{10})$	Custom application: to roughly match shear branch and cutoff frequency as mesh is refined. Danger: indefinite for certain ranges of Φ and Ψ. Use with caution.
SBM2	Shear branch matched to $O(\kappa^2)$ while flexure fitted to $O(\kappa^8)$	Custom application: to finely match shear branch and cutoff frequency as mesh is refined. Danger: indefinite for wide ranges of Φ and Ψ. Use with extreme caution.
DLMM	Diagonally lumped mass matrix with rotational mass picked to match flexural branch to $O(\kappa^6)$.	Obvious choice for explicit dynamics. Accuracy degrades significantly, however, as beam gets thicker. Underestimates frequencies. Becomes singular in the Bernoulli-Euler limit.
CDLA	Average of CMM and DLMM. Matches flexure branch to $O(\kappa^8)$.	Robust all-around choice. Less accurate than FBMS and FBMG for thin beams, but becomes top performer as aspect ratio increases. Easily constructed if CMM and DLMM available in code.
FBMG	Flexural branch matched to $O(\kappa^{10})$ with 7-parameter template (33.63).	Known to be the globally optimal positive-definite choice for matching flexure in the Bernoulli-Euler limit. Accuracy, however, is only marginally better than FBMS. As in the case of the latter, performance degrades as beam gets thicker.

§**33.7.7. *Template Instances**

Seven useful instances of the foregoing templates are identified and described in Table 33.3. Table 33.4 lists the template signatures that generate those instances. These tables include two existing mass matrices (CMM and DLMM) re-expressed in the template context, and five new ones. The latter were primarily obtained by matching series such as (33.67) and (33.68) to the continuum ones (33.48) and (33.49), up to a certain number of terms as described in Table 33.3.

For the spectral template it is possible to match the flexure branch up to $O(\kappa^{10})$. Trying to match $O(\kappa^{12})$ leads to complex solutions. For the diagonal template the choice is more restrictive. It is only possible to match flexure up to $O(\kappa^6)$, which leads to instance DLMM. Trying to go further gives imaginary solutions. For

Table 33.4. Template Signatures for Mass Matrices of Table 33.3.

Instance name	Templ. form	Template signature							Fit to continuum freqs.	
		μ_{T2}	μ_{T3}	μ_{R2}	μ_{R3}	ν_1	ν_2	μ_0	Ω_f^2 (flexural)	Ω_s^2 (shear)
CMM	(33.60)	1	1	$4\Psi^2$	$4\Psi^2$				up to κ^6	none
FBMS	(33.60)	2	26/3	$4\Psi^2+\Phi/3$	c_1				up to κ^{10}	none
SMB0	(33.60)	2	$-7/3$	$4\Psi^2+\Phi/3$	$20\Phi\Psi^2$				up to κ^{10}	up to κ^0
SMB2	(33.60)	2	$-7/3$	c_2	$20\Phi\Psi^2$				up to κ^8	up to κ^2
DLMM	(33.62)					0	$\frac{1}{2}\Psi^2$		up to κ^6	none
CDLA	(33.63)	1	1	$4\Psi^2$	$4\Psi^2$	0	$\frac{1}{2}\Psi^2$	1/2	up to κ^8	none
FBMG	(33.63)	c_3	c_4	c_5	c_6	1/12	$\frac{1}{2}\Psi^2$	c_7	up to κ^{10}	none

$$c_1 = \left(25\Phi^3 + 120\Psi^2 + \Phi^2(45 - 300\Psi^2) + 3\Phi(7 - 20\Psi^2 + 1200\Psi^4)\right)/\left(15(1 + \Phi)\right),$$
$$c_2 = \left(-19 + 10\Phi^2(90\Psi^2 - 1) - 30\Phi(1 - 26\Psi^2 + 120\Psi^4)\right)/\left(75(1 + \Phi)^2\right),$$
$$c_3 = (9 + \sqrt{105})/10, \quad c_4 = (61\sqrt{105} - 483)/18, \quad c_5 = (\sqrt{105} - 1)\Phi/30,$$
$$c_6 = \big(-48\Phi + 727\Phi^2 + 840\Phi^3 + 22128\Psi^2 + 19848\Phi\Psi^2 - 10080\Phi^2\Psi^2 - 113040\Psi^4$$
$$+120960\Phi\Psi^4 + 5\sqrt{105}(48\Phi + 87\Phi^2 + 40\Phi^3) - 24(6 + 21\Phi + 20\Phi^2)\Psi^2$$
$$+720(3 + 8\Phi)\Psi^4\big)/\big(60(21 + \sqrt{105})(1 + \Phi)\big), \quad c_7 = (3 - 5\sqrt{5/21})/8.$$

the 7-parameter template (33.63) it is again possible to match up to $O(\kappa^{10})$ but no further. The instance that exhibits least truncation error while retaining positivity is FBMG. This is globally optimal for the Bernoulli-Euler limit $\Phi = \Psi = 0$, but the results are only slightly better for the reasons discussed in 33.6.9. Matching both flexure and shear branches leads to instances SBM0 and SBM2, which have the disadvantages noted in Table 33.3.

The exact dispersion curves of these instances are shown in Figure 33.13 for $\Phi = 48/125$ and $\Psi^2 = 1/75$, which pertains to a thick beam. On examining Figure 33.13(c) it is obvious that trying to match the shear branch is difficult; the fit only works well over a tiny range near $\kappa = 0$.

§33.7.8. *Vibration Analysis Example

The performance of the seven instances of Tables 3–4 for vibration analysis is evaluated on a simply supported (SS) prismatic beam of length L divided into N_e equal elements. The cross section is rectangular with width b and height h. The material is isotropic with Poisson's ratio $\nu = 0$. Three different height-to-span ratios h/L, characterizing a thin, moderately thick and thick beam, respectively, are considered. Results for these configurations are collected in Figures 33.14, 33.15 and 33.16, respectively, for the first three vibration frequencies. All calculations are rendered dimensionless using the scaling techniques described previously.

Vibration accuracy is displayed as log-log plots of dimensionless natural frequency error versus N_e. The error is displayed as $d = \log_{10}(|\Omega_{comp} - \Omega_{exact}|)$, which gives at a glance the number of correct digits d, versus $\log_2 N_e$ for $N_e = 1$ to 32. Should the error be approximately controlled by a truncation term of the form $\propto \kappa^m$,
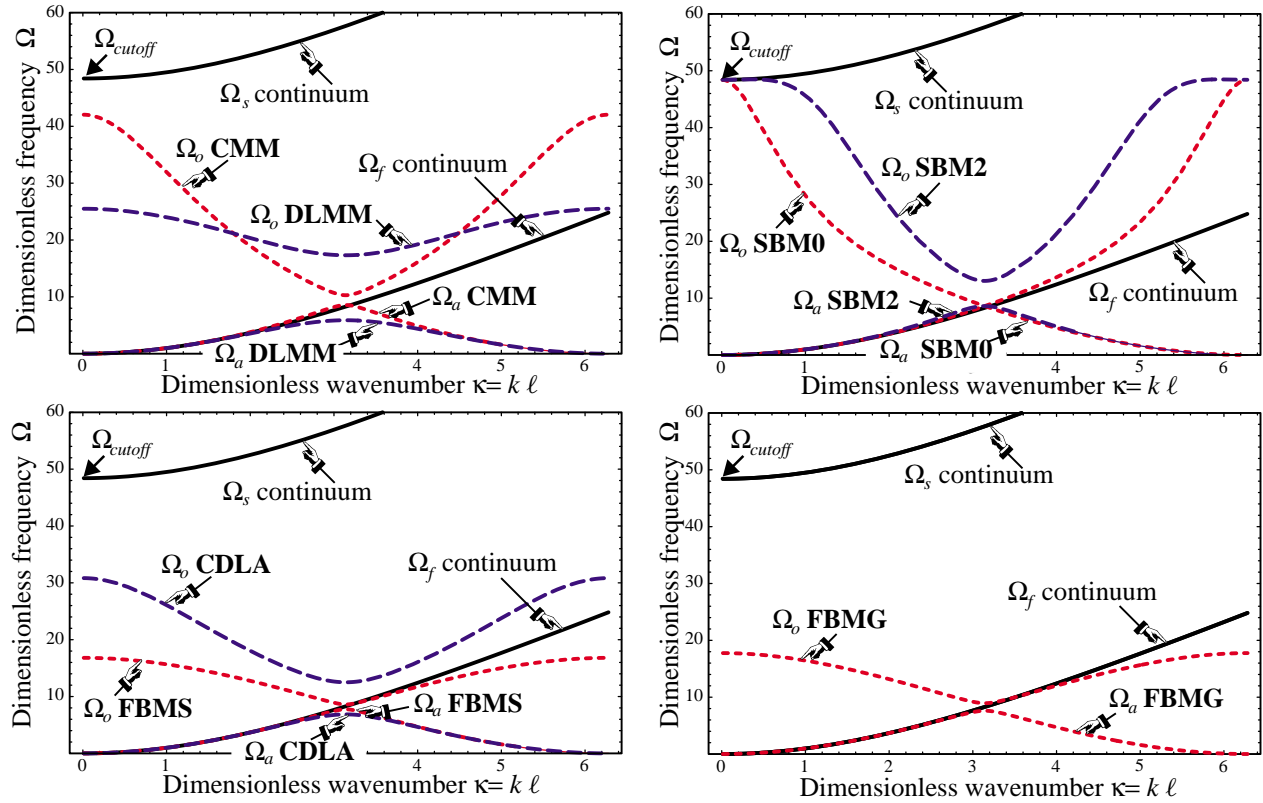
FIGURE 33.13. Dimensionless dispersion curves of Timoshenko mass matrices instances of Tables 33.3–33.4 for a thick beam with $\Phi_0 = 48/125 = 0.384$ and $\Psi_0^2 = 1/75 = 0.0133$. (a) Curves for standard consistent and diagonally-lumped matrices CMM and DLMM; (b) curves for the flexural-branch-matched FBMS and CDLA, (d) curves for the shear-branch-matched SBM0 and SBM2; (e) curve for flexure branch globally optimized FBMG.

the log-log plot should be roughly a straight line of slope $\propto m$, since $\kappa = k\ell = kL/N_e$.

The results for the Bernoulli-Euler model, shown in Figure 33.14, agree perfectly with the truncation error in the Ω_f^2 branch as listed in Table 33.4. For example, top performers FBMG and FBMS gain digits twice as fast as CMM, DLMM and SBM2, since the formers match Ω_f^2 to $O(\kappa^{10})$ whereas the latter do that only to $O(\kappa^6)$. Instances CDLA and SMB0, which agree through $O(\kappa^8)$, come in between. The highly complicated FBMG is only slightly better than the simpler FBMS. Their high accuracy case should be noted. For example, four FBMS elements give Ω_1 to six figures: $9.86960281\ldots$ versus $\pi^2 = 9.86960440\ldots$, whereas CMM gives less than three: $9.87216716\ldots$. The "accuracy ceiling" of about 11 digits for FBMS and FBMG observable for $N_e > 16$ is due to the eigensolver working in double precision (≈ 16 digits). Rerunning with higher (quad) floating point precision, the plots continues marching up as straight line before leveling at 25 digits.

On passing to the Timoshenko model, the well ordered Bernoulli-Euler world of Figure 33.14 unravels. The culprits are Φ and Ψ. These figure prominently in the branch series and grow without bound as N_e increases, as discussed in 33.6.2. Figure 33.15 collects results for a moderately thick beam with $h/L = 1/8$, which corresponds to $\Phi_0 = 3/80$ and $\Psi_0^2 = 1/768$. The Bernoulli-Euler top performers, FBMS and FBMG, gradually slow down and are caught by CDLA by $N_e = 32$. All other instances trail, with the standard ones: CMM and DLMM, becoming the worst performers. Note that for $N_e = 32$, CMM and DLMM provide only 1 digit of accuracy in Ω_3 although there are $32/1.5 \approx 21$ elements per wavelength.

Figure 33.16 collects results for a thick beam with $h/L = 2/5$, corresponding to $\Phi_0 = 24/625$ and $\Psi_0^2 = 1/75$. The foregoing trends are exacerbated, with FBMS and FBMG running out of steam by $N_e = 4$ and CDLA
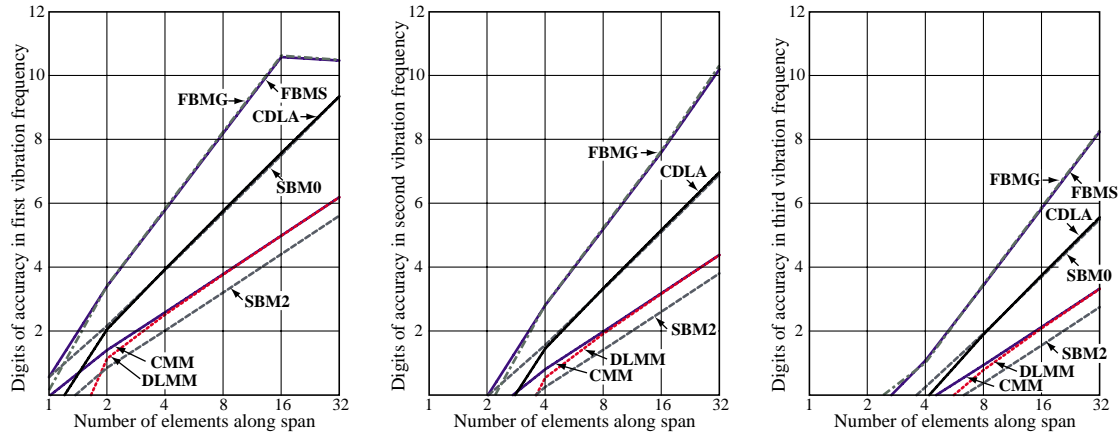
FIGURE 33.14. Accuracy of first 3 natural vibration frequencies of SS prismatic beam using mass matrices of Tables 33.3–33.4. Bernoulli-Euler model with $\Phi_0 = \Psi_0 = 0$. Exact (12-decimal) frequencies $\Omega_1 = \pi^2 = 9.869604401089$, $\Omega_2 = 4\pi^2 = 39.478417604357$ and $\Omega_3 = 9\pi^2 = 88.826439609804$. Cutoff frequency $+\infty$.
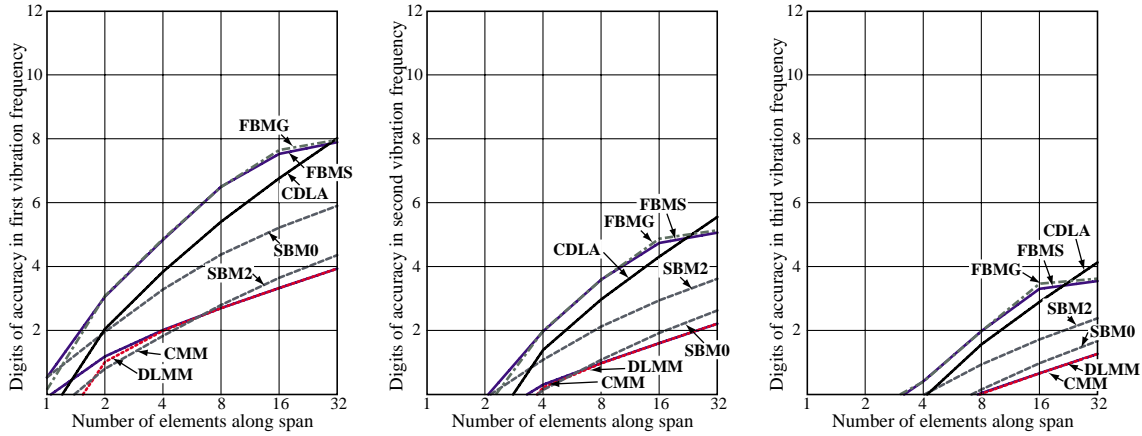

FIGURE 33.15. Accuracy of first 3 natural vibration frequencies of SS prismatic beam using mass matrices of Tables 33.3–33.4. Timoshenko model with $\Phi_0 = 3/80 = 0.0375$ and $\Psi_0^2 = 1/768 = 0.00130$, pertaining to a rectangular x-section with $h/L = 1/8$ and $\nu = 0$. Exact (12-decimal) frequencies $\Omega_1 = 9.662562122511$, $\Omega_2 = 36.507937703548$ and $\Omega_3 = 75.894968024537$. Cutoff frequency $\Omega_{cut} = 12/(\Phi_0\Psi_0^2) = 495.741868314549$.
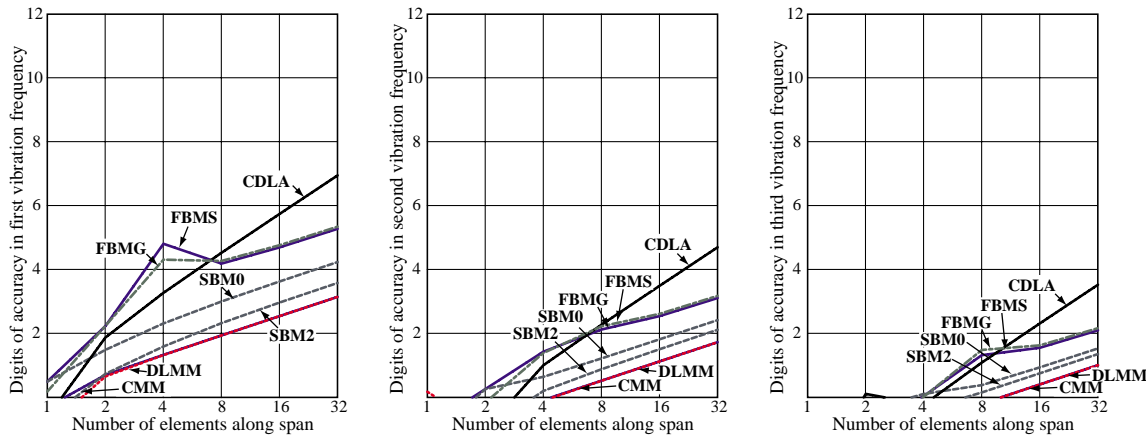

FIGURE 33.16. Accuracy of first 3 natural vibration frequencies of SS prismatic beam using mass matrices of Tables 33.3–33.4. Timoshenko model with $\Phi_0 = 24/625 = 0.384$ and $\Psi_0^2 = 1/75 = 0.0133$, pertaining to a rectangular x-section with $h/L = 2/5$ and $\nu = 0$. Exact (12-decimal) frequencies $\Omega_1 = 8.287891683498$, $\Omega_2 = 24.837128591729$ and $\Omega_3 = 43.182948411234$. Cutoff frequency $\Omega_{cut} = 12/(\Phi_0\Psi_0^2) = 48.412291827593$.

emerging as best for $N_e \geq 8$. Again DCLM and CMM trail badly.

The reason for the performance degradation of FBMS and FBMG as the Timoshenko beam gets thicker is unclear. Eigensolver accuracy is not responsible since rerunning the cases of Figures 33.15 and 33.16 in quad precision did not change the plots. A numerical study of the Ω_f^2 truncation error shows that FBMS and FBMG fit the continuum branch better than CDLA even for very thick beams. Possible contamination of vibration mode shapes with the shear branch was not investigated.

Notes and Bibliography

The template approach addresses the deficiencies of the conventional mass models by using a parametrization approach that permits customization of that matrix to the problem and solution method at hand. The method was originally developed to construct high-performance stiffness matrices; a historical account and pertinent references are provided in a recent tutorial [92]. For stiffness-mass pairs it was used in [85,88] for a Bernoulli-Euler plane beam using Fourier analysis. One idea developed in those papers but not pursued here was to include the stiffness matrix template in the customization process. This provides more flexibility but has a negative side: highly optimized stiffness-mass pairs become sensitive to mesh distortion.

The symbolic derivation scheme used for the EOM (33.45) is due to Flaggs [95]; see also [189].

Making **K** and **M** frequency dependent was first proposed by Przemieniecki [205], who expanded both $\mathbf{K}^e$ and $\mathbf{M}^e$ as Taylor series in ω^2. The idea was applied to eigenfrequency analysis of bars and beams, but not pursued further. The approach can be generalized to the template context by making free parameters frequency dependent, as illustrate in the two-node bar example. This may be of interest for problems dominated by a single driving frequency, as in some electronic and optical components. For more general use keeping the parameters frequency independent, as done in the last two examples, appears to be more practical.

Two powerful customization techniques used regularly for templates are Fourier methods and modified differential equations (MoDE). Fourier methods are limited to separable systems but can be straightforward to apply, requiring only undergraduate mathematics. (As tutorials for applied Fourier methods Hamming's textbooks [126,127], are recommended.) MoDE methods, first published in correct form in 1974 [262] are less restrictive but more demanding on two fronts: mathematical ability and support of a computer algebra system (CAS). Processing power limitations presently restrict MoDE to two-dimensional elements and regular meshes. The selection of template optimization criteria is not yet on firm ground. For example: is conservation of angular momentum useful in mass templates? The answer seems to depend on the element complexity.

Results for regular lattices of structural elements have direct counterparts in a very different area: molecular physics. More precisely, the wave mechanics of crystalline solids created in the XX Century by particle mechanicians; e.g., [35,282]. In crystal models, lattice nodes are occupied by molecules interacting with adjacent ones. Thus the "element dimension" ℓ acquires a physical meaning of molecular gap. In those applications masses are always *lumped* at molecule locations, and atoms vibrate as harmonic oscillators in the potential well of the force fields of their neighbors. Dispersion curves govern energy transmission. In a linear atomic chain, the wavenumber range $\kappa \in [-\pi, \pi]$ is called the first Brillouin zone [36,150]. Such a connection may be of interest as FEM and related discretization methods are extended into nano-mechanics.

References

Referenced items moved to Appendix R.

Homework Exercises for Chapter 33
Customized Mass Matrices of 1D Elements

EXERCISE 33.1 [A:10]. Express the Nyquist frequency for the 2-node bar lattice as function of μ.

EXERCISE 33.2 [A:30]. Investigate the behavior of an infinite 2-node bar lattice where element lengths alternate. Use either Fourier or MoDE.

EXERCISE 33.3 [A:25]. Investigate customized mass matrices for the 3-node bar without preimposing the angular moment conservation condition $\mu_1 = \mu_3$. Use Fourier analysis on a lattice, stating from a 3-parameter mass template.